Molecular Cell

Article

The human BAF chromatin remodeler processes nucleosomes bound by pioneer transcription factors OCT4–SOX2

Graphical abstract

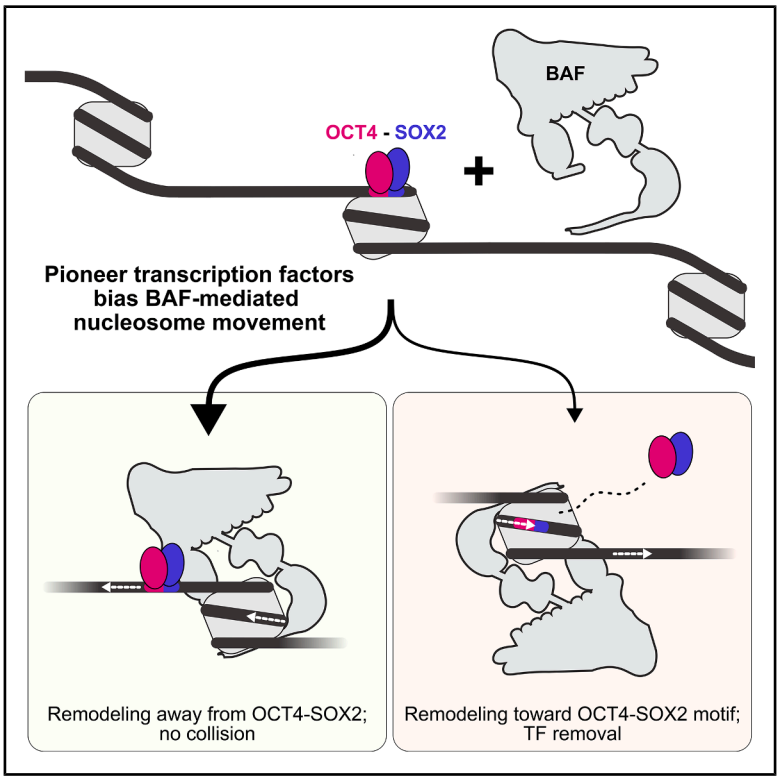

Highlights

- BAF spontaneously reverses its remodeling direction
- OCT4–SOX2 act as DNA-bound barriers that bias remodeling away from their motif
- Cryo-EM shows how BAF engages OCT4–SOX2-bound nucleosomes

Authors

Joscha Weiss, Luca Vecchia, David Domjan, ..., Michael B. Stadler, Sebastian Deindl, Nicolas H. Thomä

Correspondence

nicolas.thoma@epfl.ch

In brief

Weiss et al. structurally and functionally characterize the interplay between the human BAF chromatin remodeler and nucleosome-bound pioneer transcription factors, uncovering a highly dynamic remodeling process in which nucleosome-bound transcription factors bias the direction of BAF remodeling to regulate genome access.

Weiss et al., 2026, Molecular Cell *86*, 625–639
February 19, 2026
https://doi.org/10.1016/j.molcel.2026.01.021

CellPress

Molecular Cell

CellPress
OPEN ACCESS

Article

The human BAF chromatin remodeler processes nucleosomes bound by pioneer transcription factors OCT4–SOX2

Joscha Weiss,[1,2,3,11] Luca Vecchia,[2,11] David Domjan,[1,2,11] Simone Cavadini,[2,11] Anton Sabantsev,[4] Georg Kempf,[2] Ganesh R. Pathare,[2,6] Klaus Brackmann,[4] Alicia K. Michael,[2,7] Lukas Kater,[2] Eric Hietter-Pfeiffer,[2,8] Mina Haddawi,[2,9] Urja P. Kuber,[1] Sandra Mühlhäusser,[2] Ralph S. Grand,[2,10] Michael B. Stadler,[2,3,5] Sebastian Deindl,[4] and Nicolas H. Thomä[1,2,12,*]

[1]Institute for Cancer Research (ISREC), Swiss Federal Institute of Technology Lausanne (EPFL), Station 19, CH-1015 Lausanne, Switzerland
[2]Friedrich Miescher Institute for Biomedical Research, Fabrikstrasse 24, 4058 Basel, Switzerland
[3]University of Basel, Petersplatz 10, 4001 Basel, Switzerland
[4]Department of Cell and Molecular Biology, Science for Life Laboratory, Uppsala University, 75237 Uppsala, Sweden
[5]Swiss Institute of Bioinformatics, 4058 Basel, Switzerland
[6]Present address: Ridgeline Discovery GmbH, Technologiepark, Hochbergerstrasse 60C, 4057 Basel, Switzerland
[7]Present address: Institute of Science and Technology, Klosterneuburg, Austria
[8]Present address: Monte Rosa Therapeutics AG, WKL-136, 3, Klybeckstrasse 191, 4057 Basel, Switzerland
[9]Present address: The Walter and Eliza Hall Institute of Medical Research, Melbourne, Australia
[10]Present address: Center for Molecular Biology of Heidelberg University (ZMBH), Heidelberg University, Im Neuenheimer Feld 282, 69120 Heidelberg, Germany
[11]These authors contributed equally
[12]Lead contact
*Correspondence: nicolas.thoma@epfl.ch
https://doi.org/10.1016/j.molcel.2026.01.021

SUMMARY

Chromatin remodeling complexes mobilize nucleosomes and promote transcription factor (TF) binding. Using ensemble and single-molecule assays combined with cryo-electron microscopy (cryo-EM), we studied the interaction between pioneer TFs OCT4–SOX2 and the human BRG1/BRM-associated factor (BAF) complex on nucleosomes. BAF engages TF-bound substrates in two orientations, placing OCT4–SOX2 at either the remodeler ENTRY or EXIT site. At the ENTRY site, OCT4–SOX2 initially coexists with BAF without structural interference. However, continued DNA translocation is expected to cause collisions with bound TFs, which can trigger remodeling direction reversals or may induce TF dissociation. To accommodate TFs at the EXIT site, BAF undergoes structural rearrangements, and ensemble assays reveal a nucleosome subpopulation translocating away from TF-binding sites. Moreover, single-molecule experiments show that nucleosome-bound BAF frequently changes remodeling direction, and we identify an ADP-bound remodeler conformation as a potential intermediate. Together, these findings reveal key aspects of the conformational dynamics and remodeling outcomes underlying BAF processing of TF-bound nucleosomes.

INTRODUCTION

The repeating nucleosome units in chromatin limit access to genomic DNA and act as a barrier for transcription factor (TF) binding.[1,2] When faced with nucleosome-embedded DNA motifs *in vitro*, most TFs tested bind, albeit with lower apparent affinity compared with free DNA.[3] Those TFs engaging nucleosomal DNA predominantly bind solvent-exposed motifs near the nucleosomal entry/exit sites (end binders).[3,4] One of the best-studied examples is the mammalian pluripotency factors OCT4 and SOX2, pioneer factors shown to exhibit highly synergistic end-binding behavior in biochemical assays and within mouse embryonic stem cells.[5–8]

While TFs can engage nucleosomes *in vitro, in vivo* they typically reside in nucleosome-depleted regions (NDRs) of the genome.[9,10] Current models invoke TF-mediated recruitment of chromatin remodeling complexes, including the SWI/SNF (switch/sucrose non-fermentable) family of remodelers, which subsequently slide or evict nucleosomes to generate nucleosome-depleted binding sites.[11,12] The hematopoietic TF PU.1, for example, exhibits cell-fate-changing pioneering properties[13–15] while also being dependent on remodeling complexes to modulate chromatin structure.[15,16] Although PU.1 can interact

with its target sites independent of chromatin remodelers, small molecule SWI/SNF inhibitors impair the formation of NDRs around PU.1 binding sites and reduce expression of PU.1-controlled genes.[16] Similar functional cooperations between SWI/SNF members and TFs have been described for other pioneer factors, including OCT4–SOX2.[11,17–28] Beyond their essential role in generating NDRs, SWI/SNF remodelers are crucial for retaining TFs at binding sites and for maintaining the surrounding chromatin in an open state.[19,28] Interactions of TFs and remodelers with chromatin are transient,[29,30] and TFs themselves are also subject to remodeling and remodeler-dependent removal.[31] How remodelers and TFs interplay to govern TF occupancy at promoters and enhancers is currently unclear.[32]

Chromatin remodeling complexes are grouped into evolutionary conserved subfamilies, each centered on a unique ATPase core and accompanied by accessory subunits that confer target specificity and functional diversity.[33–37] In humans, the 29 SWI/SNF subunits give rise to three main configurations: canonical BRG1/BRM-associated factor (BAF), polybromo-associated BAF (PBAF), and non-canonical BAF (ncBAF).[38] BAF is the most abundant and highly mutated remodeling complex in human cancers.[39] Despite considerable subunit variability, SWI/SNF remodelers share a conserved modular organization, comprising a DNA-translocating ATPase module, a histone-engaged BASE module, and an actin-related protein (ARP) module, which bind nucleosomes by multiple interaction sites.[40–48] Binding sites on nucleosomal DNA are denoted with reference to superhelix locations (SHLs), with the dyad defined as SHL0 and the minor grooves facing the histone core from the dyad to the entry/exit sites numbered as SHL ± 1–7 (Figure S1A).[2] The ATPase catalytic domain engages and translocates nucleosomal DNA near SHL ± 2, a position conserved across SWI/SNF, ISWI, and CHD1 remodelers.[49–53] Recent structural and functional studies detail how ATP hydrolysis-driven conformational changes of the ATPase lobes pull DNA in 1 bp steps from the nucleosome entry site toward SHL2, creating torsional strain that drives DNA propagation to the dyad and release at the distal exit site.[54–59] BAF "sandwiches" the nucleosome (Figure S1C) with the C-terminal region of the ATPase (SnAC/post-SnAC) occupying one nucleosomal acidic patch, and the BASE module subunit BAF47 (SMARCB1) contacting the opposite face. The ARP module is located near SHL ± 6, close to the ends of the nucleosomal DNA. Comparison of this SWI/SNF chromatin remodeler footprint with that of nucleosome-bound TFs, for example OCT4–SOX2, reveals potential structural overlaps (Figure S1D). Similar clashes between TFs and SWI/SNF remodelers are in principle expected for most end-binding TFs on nucleosomes.[4,60]

To investigate how remodelers read out TF-bound nucleosomes and crosstalk with DNA-binding proteins, we performed *in vitro* ensemble and single-molecule chromatin remodeling reactions and solved the corresponding cryo-electron microscopy (cryo-EM) structures of nucleosome-bound OCT4–SOX2 in the presence of the human BAF chromatin remodeling complex. This uncovered a highly dynamic remodeling process in which BAF frequently changes the direction of nucleosome movement and where pioneer TFs OCT4–SOX2 impact the remodeler activity and directionality. In line with the observed functional plasticity, cryo-EM reveals a remarkable structural flexibility of the remodeler, allowing for simultaneous binding of TFs and BAF to a single nucleosome. Together, our structural and functional data provide important insights into the mechanistic crosstalk between TFs and chromatin remodelers.

RESULTS

To study how SWI/SNF chromatin remodeling complexes are impacted by nucleosome-bound TFs, we first characterized the dynamics of remodeler-catalyzed nucleosome movement in the absence of bound factors. Asymmetric nucleosomes, containing a Cy3-labeled H2A–H2B dimer, were assembled on a Widom 601 positioning sequence,[61] inserting the nucleosome adjacent to a matching fluorescence resonance energy transfer (FRET)-acceptor dye (Cy5) at the DNA end (Figures 1A, S2A, and S2B). The 601 sequence is inherently asymmetric, consisting of two half-sides with differing histone-DNA interaction strengths[62] (Figure S1G). In this bulk assay setup, remodeling by the endogenously purified human BAF complex (see STAR Methods; Figure S1B) led to a time-dependent decrease in FRET signal (Figure 1A), consistent with overall nucleosome movement away from the FRET-acceptor fluorophore, toward the longer linker and across the weaker 601 half-side (a direction we designate as the 3' DNA end from here on).

The observed nucleosome movement, as evident by a decrease in FRET efficiency, either arises from nucleosomes slowly moving toward their equilibrium positions or from a more rapid, dynamic back-and-forth movement. Both processes can give rise to similar net histone core shifts and to indistinguishable equilibrium positions. To differentiate between the two, we monitored remodeling dynamics at the single-molecule level. Labeled nucleosomes were immobilized on a polyethylene glycol (PEG)-coated quartz surface using a biotin anchor attached to the DNA end opposite of the FRET-acceptor fluorophore[63] (Figures 1B and S2B), and fluorescent signals were monitored by total-internal-reflection fluorescence (TIRF) microscopy. Interestingly, we observed that the majority (80%) of single-molecule remodeling traces initially showed a decrease in FRET efficiency, in line with remodeling away from the FRET acceptor, to subsequently reverse direction and return to higher FRET values (Figures 1C and 1E). In many cases, these spontaneous direction changes occurred repeatedly within the same remodeling trace (Figures 1C and S2C), suggesting a highly dynamic and reversible remodeling process driven by nucleosome sliding rather than eviction. Given the pseudosymmetric nature of the nucleosome, the catalytic lobes of the remodeler ATPase can engage nucleosomal DNA either at SHL + 2 or SHL − 2. The direction of nucleosome movement, in turn, depends on which of the two SHLs is engaged. One possible explanation for the observed directional changes in single-molecule experiments, hence, is frequent dissociation of the remodeler from one SHL ± 2 position, followed by re-engagement of a different BAF molecule to the other SHL ± 2 (Video S1). Alternatively, the reversal could occur within a single BAF binding event, where a bound remodeler switches the ATPase location from SHL + 2 to SHL − 2 (or *vice versa*) without complete dissociation

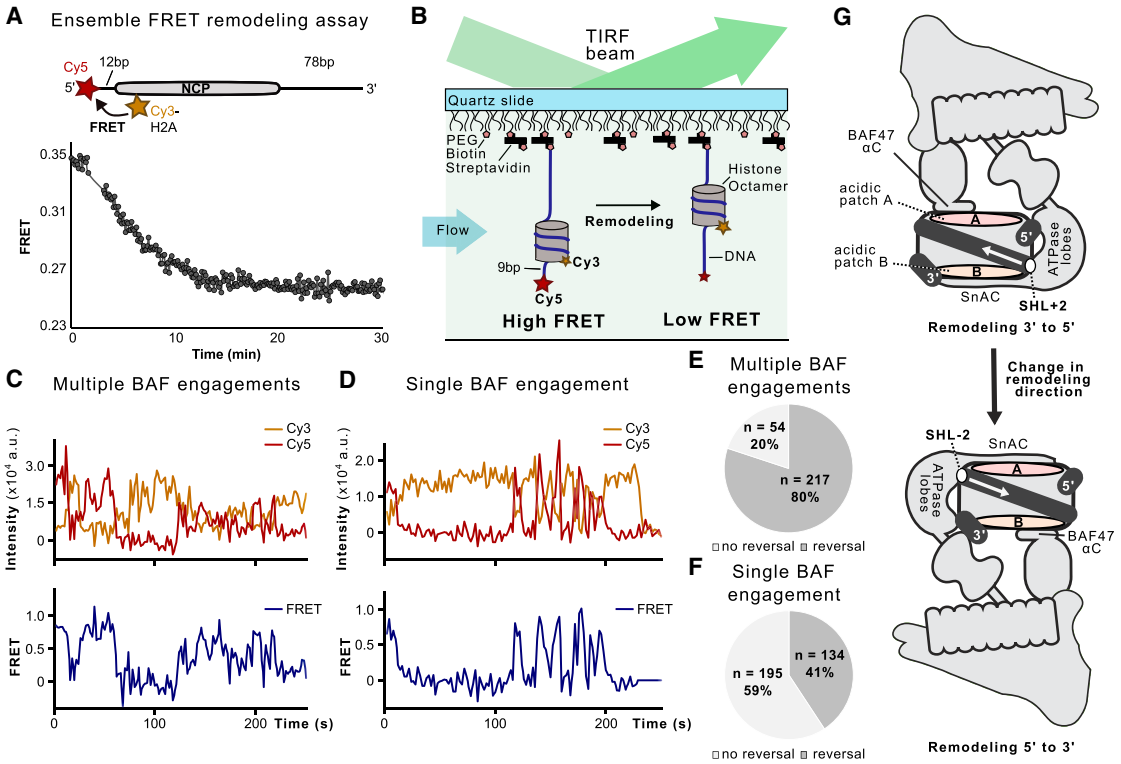

Figure 1. BAF frequently changes the direction of nucleosome movement

(A) Ensemble FRET experiment probing nucleosome sliding by the human BAF complex. Asymmetric nucleosomes containing a Cy3-labeled H2A-H2B dimer are positioned 12 bp from the Cy5 FRET-acceptor fluorophore at the 5′ DNA end. Incubation with human BAF results in a time-dependent decrease of FRET signal, in line with nucleosome movement toward the longer linker (78 bp).

(B) Experimental setup for single-molecule remodeling experiments. Nucleosomes were immobilized on a PEG-coated quartz slide using a biotin anchor, and fluorescent signals were monitored using a TIRF microscopy setup.

(C) Representative trace from a single-molecule remodeling experiment with BAF in solution, displaying transitions between high and low FRET efficiency states. The upper panel shows the raw Cy3 and Cy5 fluorescence intensities, while the lower panel depicts the corresponding FRET efficiency over time.

(D) Same as (C) but performed under conditions that restrict remodeling to a single BAF binding event. Remodeler is pre-bound to surface-immobilized nucleosomes in the presence of ATP, but without Mg^{2+}. Unbound BAF molecules in solution are washed away with the reaction buffer (containing ATP but without Mg^{2+}), and the reaction is initiated by filling the flow chamber with the reaction buffer supplemented with both ATP and Mg^{2+}.

(E) Quantification of single-molecule FRET experiments shown in (C). 80% of traces exhibit at least one direction reversal event (217 out of 271 remodeling traces).

(F) Quantification of single-molecule FRET experiments shown in (D). 41% of traces exhibit at least one direction reversal event (134 out of 329 traces).

(G) Schematic representation of BAF reversing the direction of nucleosome movement. The ATPase lobes shift from SHL + 2 to SHL − 2, while BAF47 relocates from acidic patch A to B, and the ATPase SnAC domain switches from acidic patch B to A.

(Video S2), resulting in nucleosome movement in the opposite direction. To distinguish between these scenarios, we carried out single-molecule FRET experiments allowing for only a single BAF-nucleosome engagement event while preventing re-association of dissociated or external BAF molecules. To this end, complexes between nucleosomes and remodelers were preformed in the presence of ATP but absence of $MgCl_2$, and unbound free BAF was removed in the microfluidic setup by flushing the flow channel. The remodeling reaction was subsequently initiated by a single buffer exchange to a solution containing $MgCl_2$, after which data were acquired under no-flow conditions. Strikingly, in this setup, we retained a significant fraction (41%) of single-molecule remodeling traces that change directionality (Figures 1D, 1F, and S2D). Considering the removal of unbound and excess remodeler complexes, these results support the ability of BAF to change remodeling directionality without full dissociation from the nucleosome. Such changes in directionality are frequent events, occurring at least once in nearly half of all productive remodeling traces. We cannot formally exclude the possibility that rapid rebinding of the same BAF molecule after dissociation contributes to some reversal events. However, given the restricted availability of free remodelers in this assay, we consider a reorientation mechanism that does not involve complete dissociation as the predominant pathway under our experimental conditions. Notably, the residence times of nucleosome-bound BAF observed here often exceed those reported *in vivo*[29,64] (<30 s) but align well with previous single-molecule studies on other remodelers using DNA and mono-nucleosome substrates.[65]

To reverse the direction of nucleosome sliding, the ATPase driving the DNA translocation must relocate to its pseudo-symmetric binding site on the nucleosome. Since BAF has additional

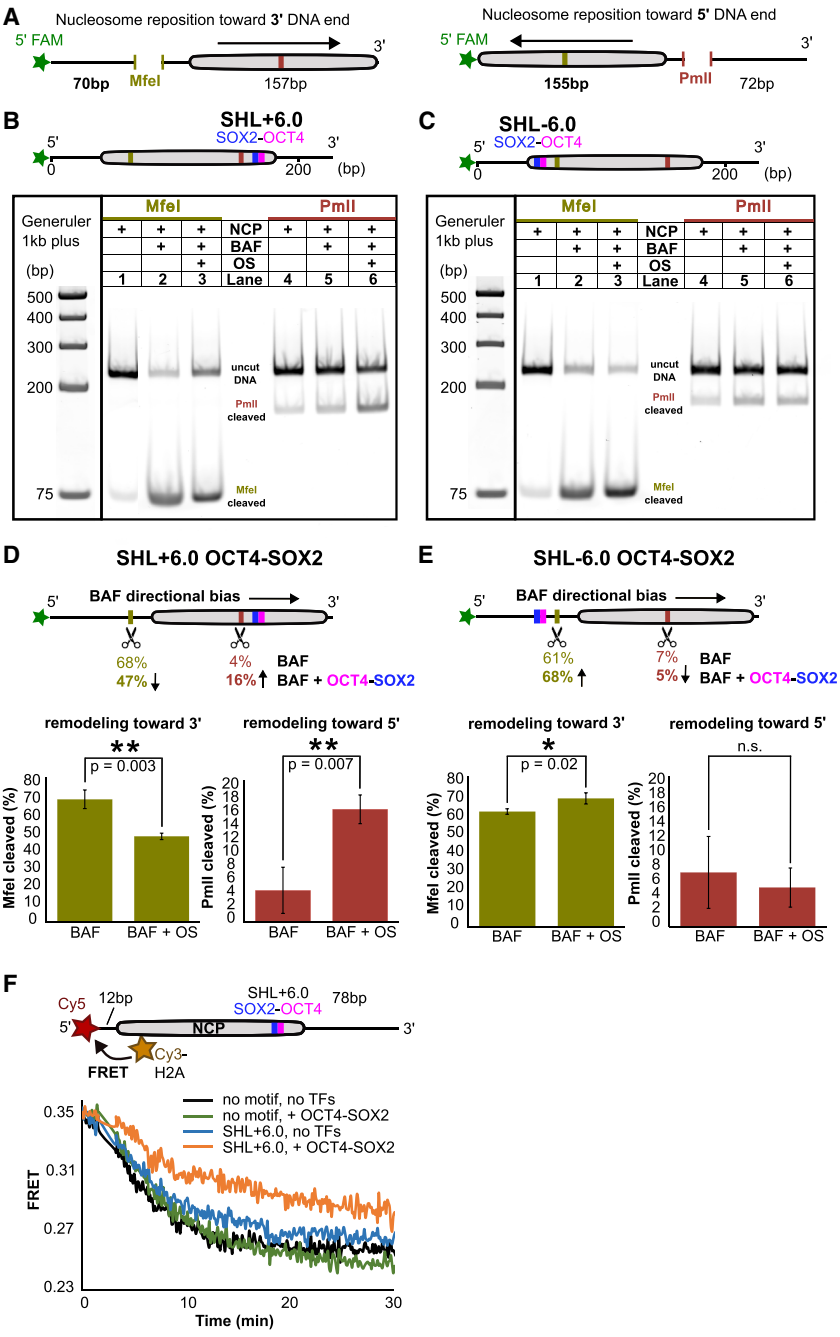

Figure 2. OCT4–SOX2 influences the direction of BAF-catalyzed nucleosome movement

(A) Schematic representation of nucleosome substrates used in restriction enzyme-based remodeling assays. A 3′ shift of the nucleosome exposes the MfeI site, producing a labeled 70 bp DNA fragment and an unlabeled 157 bp fragment. Conversely, a 5′ shift exposes the PmlI site, yielding a labeled 155 bp fragment and an unlabeled 72 bp fragment.

(B) Restriction-based remodeling assay of SHL + 6.0-motif-containing nucleosome. The gel shows fluorescently labeled DNA fragments resulting from remodeling reactions with simultaneous restriction enzyme digestion. NCP, nucleosome core particle; OS, OCT4-SOX2.

(C) Same as (B) with nucleosomes containing the motif at SHL − 6.0.

(D) Quantification of remodeling assays from (B). Mean values ± SD of restriction enzyme cleavage were calculated from the uncut band intensities and normalized to the control condition without BAF and TFs (lane 1 or 4). Mean values are based on three independent replicates ($n = 3$). Statistical significance was assessed using an unpaired two-tailed t test. $^{*}p < 0.05$, $^{**}p < 0.01$.

(E) Quantification of remodeling assays from (C). Statistical analysis was performed as in (D).

(F) Ensemble FRET remodeling assay using nucleosomes either lacking a motif or containing the composite OCT4–SOX2 motif at SHL + 6.0. Fluorescence signals were recorded over 30 min in the presence or absence of OCT4–SOX2, and FRET efficiency is plotted in the graph.

contact points with the histone core, a directional switch also implies the rearrangement of these interactions. Hence, BAF47 must shift from acidic patch A to B, while the ATPase C-terminal domains (SnAC/post-SnAC) in turn relocate from B to A (Figure 1G).

OCT4–SOX2 affects the directionality of BAF nucleosome movement

To explore the impact of TFs on nucleosome translocation dynamics, we used a restriction enzyme-based remodeling assay, which allowed monitoring of bidirectional nucleosome movement. Building on a prior study describing the nucleosome-binding properties of the pluripotency TFs OCT4–SOX2,[8] we assembled nucleosomes with the TF composite motif at either SHL − 6.0 or SHL + 6.0. These nucleosomes were flanked by 40 bp DNA overhangs on both sides of a centered nucleosome positioning sequence. To monitor nucleosome movement bidirectionally, we introduced two restriction enzyme sites: an MfeI site positioned 30 bp into the stronger half of the 601 sequence, which becomes accessible following a 3′ shift of the nucleosome onto the linker DNA, and a PmlI site positioned 32 bp into the weaker half-side, exposed following a 5′ shift of the nucleosome (Figure 2A). In the absence of OCT4–SOX2, we observe a strong increase of MfeI digestion, with negligible PmlI cleavage following 30 min of BAF-mediated remodeling with simultaneous restriction enzyme digest (Figure 2B, compare lane 1 with lane 2 and lane 4 with lane 5). This indicates a preferred shift of nucleosomes toward the 3′ DNA end. Since the linker DNA lengths are identical on both sides of the nucleosomes, this directional bias is likely governed by the intrinsic asymmetry of the Widom 601 sequence, with BAF preferentially shifting nucleosomes toward the weaker half-side. Similar

asymmetric movement of nucleosomes on Widom 601 templates has been previously reported for a related SNF2-type remodeler.[62]

We then added OCT4–SOX2 to the remodeling reaction with nucleosomes containing the TF motif at SHL + 6.0. This resulted in a reduction of MfeI digestion by ~21% (Figure 2B, compare uncut DNA in lanes 2 and 3; Figure 2D), in line with decreased nucleosome movement toward the 3′ end. TFs hence function as DNA-bound barriers that reduce BAF-mediated nucleosome movement over the TF-binding site. Concomitantly, the efficiency of PmlI cleavage increased by ~12% in the presence of OCT4–SOX2 (Figure 2B, compare lanes 5 and 6; Figure 2D), consistent with more overall nucleosome movement toward the 5′ end in the presence of TFs. OCT4–SOX2 thus partially opposes the directional remodeling preference and triggers a change in directionality. The full extent of their impact on BAF-mediated nucleosome movement is likely camouflaged by the intrinsic bias imposed by the Widom 601 sequence. Accordingly, TF-induced remodeling away from the TF site was also observable with nucleosomes containing the OCT4–SOX2 motif at SHL − 6.0 (Figures 2C and 2E), yet here the influence of the TFs is reduced, as nucleosome movement away from the TF motif is already aligned with the directional bias of BAF remodeling. Together, these data suggest that TFs can act as DNA-bound barriers, modulating nucleosome movement by BAF and introducing a TF-induced directional preference, reflected by a subset of nucleosomes moving away from the TF-binding site. We anticipate that the observed 12% effect, when extrapolated genome-wide, will significantly impact gene regulatory regions.

To further quantify the ability of TFs to serve as roadblocks, we carried out ensemble FRET experiments assessing BAF-induced nucleosome sliding in the presence and absence of TFs. The OCT4–SOX2 motif was introduced at SHL + 6.0 and is positioned such that it faces the long linker DNA (Figures 2F, S2A, and S2E). Thus, to mobilize nucleosomes toward the 3′ end of the DNA template, as observed in Figure 1A, BAF would have to shift nucleosomes toward the OCT4–SOX2 binding site. Fluorescence signals were recorded for 30 min during these ensemble remodeling experiments. To account for unspecific binding of OCT4–SOX2, nucleosomes lacking a TF motif served as a negative control. Experiments with or without TFs showed a reduction of FRET efficiency over time, consistent with an overall nucleosome movement toward the 3′ DNA end (Figure 2F). In the presence of OCT4–SOX2 with the composite motif at SHL + 6.0, however, the decrease in FRET efficiency was markedly slower, indicating reduced nucleosome sliding toward the longer linker (Figure 2F). Although OCT4–SOX2 does not completely block BAF-mediated nucleosome movement toward the TFs motif, a significant decrease in the change of FRET efficiency is observed following 20 min of remodeling in the presence versus the absence of the TFs (Figure S1E). This effect is specific to OCT4–SOX2 binding to SHL + 6.0, as no impact of TF addition was observed for nucleosomes lacking a TF motif (Figure 2F). These findings suggest that OCT4–SOX2 bound at the edges of the nucleosome reduces sliding toward the TFs yet does not entirely abolish histone octamer movement in that direction.

This in turn raises the intriguing possibility that BAF can tolerate a TF bound at the DNA ENTRY site of the remodeler-nucleosome complex, although nucleosome translocation across the TF-binding site is expected to ultimately lead to TF collision and displacement. To gain further mechanistic insights into the TF/BAF interplay, we determined structures of complexes formed between BAF and nucleosomes bound by OCT4–SOX2.

BAF nucleosome engagement places TFs at the ENTRY site

We first solved a cryo-EM structure of the remodeler-bound nucleosome in the presence of pioneer factors OCT4–SOX2 at SHL − 6.0. Unless otherwise stated, samples for cryo-EM were prepared in the presence of the non-hydrolysable ATP analog, adenyl-5′-yl imidodiphosphate (AMP-PNP), followed by chemical cross-linking in gradient fixation (GraFix) using glutaraldehyde.[66] Cryo-EM structure determination revealed densities for both BAF and OCT4–SOX2 located on the same nucleosome. Thus, binding of both transcriptional regulators to nucleosomes is not mutually exclusive, a finding further confirmed under non-crosslinking conditions in electrophoretic mobility shift assays (EMSA) (Figure S1F). The cryo-EM map was refined to an overall resolution of 3.5 Å, with subsequent local refinements on nucleosome-OCT4/SOX2-ATPase yielding 3.2 Å and 2.9 Å maps, and local refinement on the BASE and ARP modules giving a 3.1 Å reconstruction (Figure S3; Table 1) (see STAR Methods). Local resolutions were between 2.5 and 5 Å for the BASE, ARP, and the nucleosome, and between 7 and 10 Å for the ATPase and TFs (Figures S3D, S3E, and S3F).

Density for OCT4–SOX2 in this cryo-EM map can be found at the ENTRY site of the remodeler-nucleosome complex (Figures 3A and 3B), without evidence for direct interactions between the TFs and BAF. Comparison to the published structure of OCT4–SOX2 at SHL − 6.0 in the absence of the remodeler[8] finds the TF-nucleosome module largely unaffected by the presence of BAF (Figure S4A). Furthermore, the remodeler engages the nucleosome in a conformation that resembles previously solved structures of nucleosome-bound BAF in the absence of TFs[40,41] (Figure S4B). The ATPase catalytic domain engages nucleosomal DNA near SHL − 2.0 (Figures 3A and S4C), while the C-terminal SnAC domain of the BRG1/BRM (SMARCA2/4) ATPase gave rise to a defined cryo-EM density, engaging acidic patch A of the nucleosome and sitting in proximity of the SOX2 HMG domain (Figures 3C and S4C). The αC helix of BAF47 as part of the HEAD submodule of BASE[40] engages acidic patch B of the nucleosome (Figure S4C). The structured core of the BASE module also gave rise to a defined density, highlighting the strongly interwoven assembly of different subunits of the BAF complex (Figures 3A and S4D). In addition, we observed density consistent with the β-stranded YEATS-like domain of BAF60 (SMARCD) in the BASE module, not modeled in previous BAF structures (Figure S4D).

Our cryo-EM structure reveals that BAF can engage TF-bound nucleosomes, circumventing potential structural clashes between the TFs and the ARP module/HSA (helicase-SANT-associated) helix of the remodeler by placing the TFs at the ENTRY site. Taking into consideration the mechanism of DNA translocation by the BAF ATPase from a fixed location at SHL − 2 toward

Table 1. Statistics of cryo-EM data collection and refinement

	BAF-OS^{+6} class 1	BAF-OS^{+6} class 2	BAF-OS^{+6} ADP	BAF-OS^{-6}
Data collection and processing				
Detector	Falcon 4i	Falcon 4i	Falcon 4i	Falcon 4i
Magnification	75,000	75,000	75,000	75,000
Voltage (kV)	300	300	300	300
Electron exposure (e–/Å2)	50	50	50	50
Defocus range (μm)	−0.5 – −2.5	−0.5 – −2.5	−0.5 – −2.5	−0.5 – −2.5
Pixel size (Å)	0.845	1.69	0.845	0.845
Symmetry imposed	C1	C1	C1	C1
Initial particle images (no.)	5,154,573	5,154,573	2,420,264	1,744,128
Final particle images (no.)	30,808	27,074	83,832	179,373
Consensus map resolution (Å)	4.2	4.1	5.9	3.5
Local refinement, base module (Å)[a]	4.0		6.5	3.1
Local refinement, NCP module (Å)[a]	3.3		4.05	2.9
Local refinement, ARP module (Å)[a]				3.7
FSC threshold	0.143	0.143	0.143	0.143
Map resolution range (Å)	3–20	3–20	3–20	3–10
Refinement				
Initial models used (PDB codes)	6YOV, 6LTJ	6YOV, 6LTJ	BAF-OS^{+}6 class 1 + 7VDT	6T90, 6LTJ, and 7VDT
Map sharpening B factor (Å2)	N/A.	N/A.	N/A.	N/A.
Model composition				
Non-hydrogen atoms	27,965	23,423	29,773	38,125
Protein residues	3,626	3,092	4,202	4,342
Nucleotides	262	276	268	284
Ligands	1	0	0	17
B factors (Å2)	260.18	352.37	477.45	158.45
Protein	258.81	411.11	516.58	147.78
DNA	265.99	167.96	304.55	218.65
Root mean square (RMS) deviations				
Bond lengths (Å)	0.006	0.009	0.005	0.006
Bond angles (°)	1.057	1.355	0.978	1.146
Validation				
MolProbity score	0.89	0.98	0.94	0.77
Clashscore	0.46	0.91	0.63	0.40
Poor rotamers (%)	0.52	0.28	0.30	0.49
Ramachandran plot				
Favored (%)	96.49	96.77	96.44	97.35
Allowed (%)	3.42	3.10	3.39	2.56
Disallowed (%)	0.08	0.13	0.17	0.09
Model-to-data fit[b]				
CCmask	0.6739	0.6651	0.7845	0.8337
CCbox	0.8353	0.7348	0.8468	0.8696
CCpeaks	0.5312	0.5903	0.6082	0.7468
CCvolume	0.6550	0.7057	0.7818	0.8257

[a]Local refined cryo-EM maps used to build the composite map in Chimera (vop maximum).
[b]Map-model correlation coefficients (Phenix v1.20.1-4487) calculated using the model fitted into the composite cryo-EM map.

the nucleosome dyad (Figure S4C), this predicts that BAF-mediated DNA translocation toward the TF motif ultimately results in steric clashes, potentially leading to TF removal via BAF-induced remodeling. While we indeed observed a slowdown or stalling of nucleosome translocation toward the TFs binding site (Figure 2F), we also found a subpopulation of nucleosomes

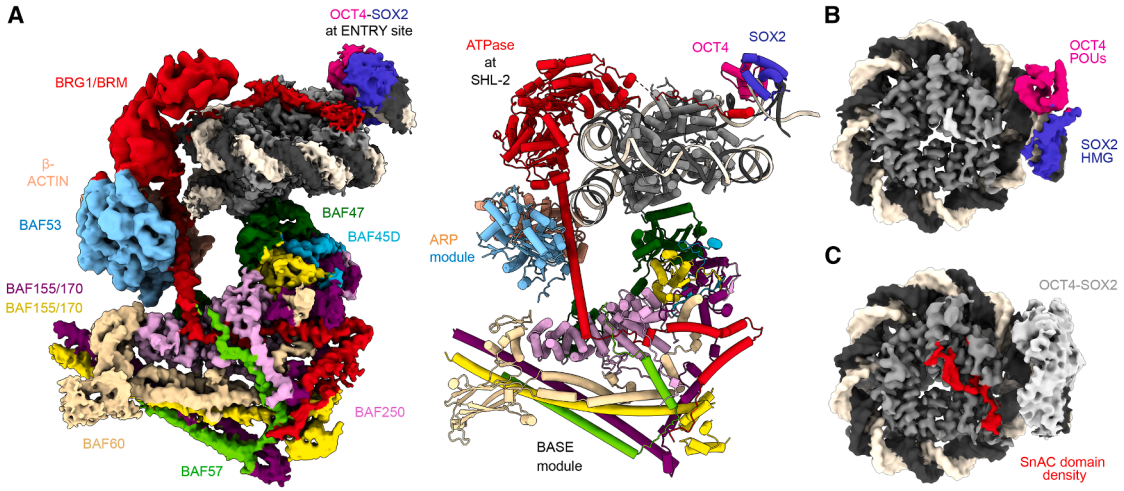

Figure 3. BAF engages the OCT4–SOX2 SHL – 6.0 nucleosome in an orientation that places the TFs at the ENTRY site

(A) Composite cryo-EM map and model of BAF-OS$^{SHL-6.0}$ colored by subunit. Density for OCT4–SOX2 can be found at the ENTRY site of the remodeler-nucleosome complex.

(B) Cryo-EM map of a focused classification on the TF-bound nucleosome, highlighting the density of the OCT4 POUs DNA binding domain and the SOX2 HMG domain.

(C) Cryo-EM map of a focused classification on the TF-bound nucleosome, highlighting the density of the ATPase SnAC domain meandering on the nucleosome acidic patch.

moving in the opposite direction in restriction-based remodeling experiments (Figures 2B–2E). This demonstrates that BAF can translocate nucleosomes away from DNA-bound factors and suggests the existence of a directionality inversion point following initial BAF engagement and TF translocation toward the nucleosome.

BAF can also accommodate OCT4–SOX2 at the EXIT site

To better understand the potential modes of BAF engagement with TF-nucleosome complexes, we turned our attention to a second nucleosome substrate carrying the composite OCT4–SOX2 motif at SHL + 6.0 (another location formerly characterized structurally).[8] Here, the TF motif orientation is inverted compared with the SHL − 6.0 position, with SOX2 facing the nucleosome dyad and OCT4 pointing toward the DNA end (Figure S1G). Once again, cryo-EM structure determination revealed densities for both BAF and OCT4–SOX2 located on the same nucleosome. In this dataset, however, we could distinguish between two binding modes in 2D and 3D classifications. The first 3D class (BAF-OS$^{+6.0}$ class 1) shows the TFs positioned at the ENTRY site of the remodeler-nucleosome complex (Figure 4), consistent with the BAF-OS$^{-6.0}$ structure presented above. Surprisingly, in the second 3D class (BAF-OS$^{+6.0}$ class 2), OCT4–SOX2 is positioned proximal to the remodeler at the nucleosome EXIT site, and BAF underwent large, albeit localized, conformational changes to accommodate the TFs (Figure 5). The number of particles assigned to both 3D classes is roughly comparable (Figures S5 and S7), indicating that the two distinct binding modes exist in equilibrium.

Class 1 was solved to an overall resolution of 3.8 Å in conventional refinement and of 4 Å in 3D Flex flexible refinement[67] performed in cryoSPARC 4.1 (Figure S5; Table 1) (see STAR Methods). In conventional refinement, local resolutions ranged from 3 to 7 Å for the nucleosome and 8 to 20 Å for the ARP module, the ATPase, and the TFs (Figure S5B). In flexible refinement, the reported resolution ranged from 3 to 5 Å for the nucleosome and 7 to 20 Å for the ARP module, the ATPase, and the TFs (Figure S5C). Density for the SHL + 6.0-bound TFs OCT4–SOX2 can be found at the ENTRY site of the remodeler-nucleosome complex, supporting simultaneous binding of both transcriptional regulators to the same nucleosome without direct physical contacts (Figures 4A and 4B). The TF-nucleosome module again remains largely unaffected by the presence of BAF (Figure S6A) and closely resembles the published OCT4–SOX2 nucleosome structure in the absence of the remodeler.[8] As a result of the altered location of the TFs motif, BAF binds the nucleosome in an inverted orientation compared with the BAF-OS$^{-6.0}$ structure (Figures 4B and 4C), with the ATPase catalytic lobes engaging nucleosomal DNA around SHL + 2.0 (instead of SHL − 2.0 in BAF-OS$^{-6.0}$). Since OCT4–SOX2 is again positioned at the nucleosome ENTRY site, ATPase-driven DNA translocation would result in a directed movement of the TFs into the nucleosome core. In addition to the ATPase catalytic domain, the ARP module, the HEAD submodule of the BASE, and the armadillo repeats domain (ARM) region of BAF250 (ARID1) could also be fitted in the density, while other BASE subunits could not be reconstructed, likely because of flexibility, as is evident in 3D Flex analysis (Figure S6B; Videos S3 and S4). Overall, the structure observed in class 1 closely mirrors the configuration obtained with OCT4–SOX2 at SHL − 6.0, and the functional consequences—namely, TF-directed translocation into the nucleosome core and collision—remain consistent.

Class 2 was solved at an overall resolution of 4.2 Å. Following local refinement, the ATPase, nucleosome, and OCT4–SOX2 were refined to 3.3 Å resolution, while the ARP and BASE

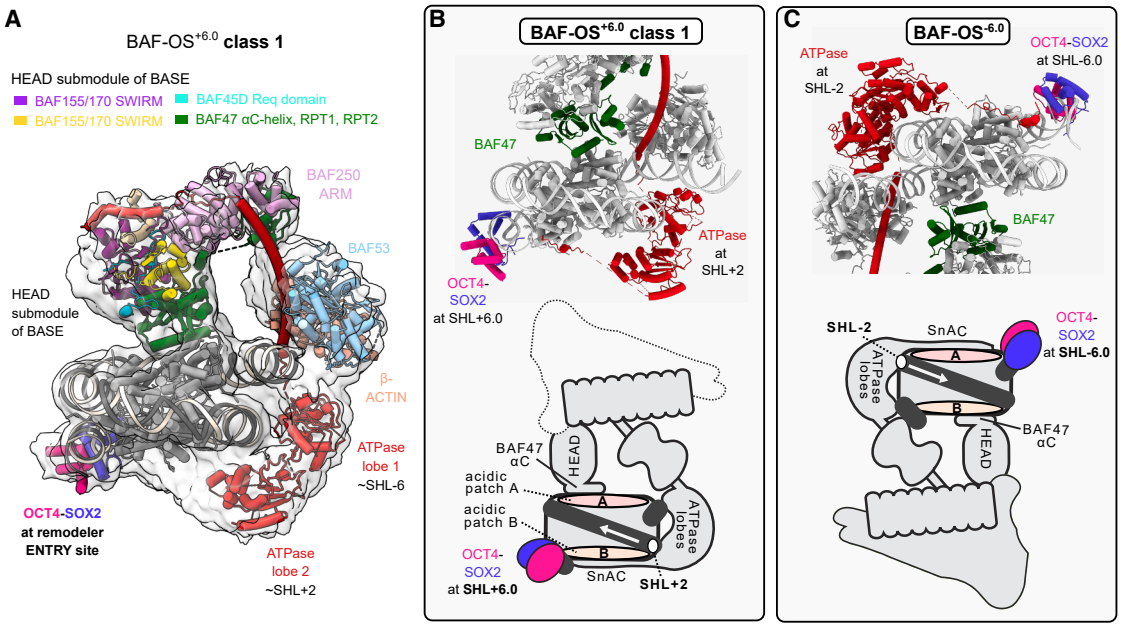

Figure 4. Class 1 structure of BAF bound to the SHL + 6.0 nucleosome, showing OCT4–SOX2 positioned at the ENTRY site

(A) Overlay of cryo-EM map in gray and model of BAF-OS$^{SHL+6.0}$ class 1 colored by subunit. ARM, armadillo repeats domain; SWIRM, SWI3/RSC8/MOIRA domain.

(B) Focused view of the cryo-EM model on the nucleosome and schematic representation of the BAF-OS-nucleosome complex highlighting the engagement orientation of the remodeler in BAF-OS$^{+6.0}$ class 1. The white arrow indicates the direction of DNA translocation toward the nucleosome dyad.

(C) Focused view of the cryo-EM model on the nucleosome and schematic representation of the BAF-OS-nucleosome complex highlighting the engagement orientation of the remodeler in BAF-OS$^{-6.0}$. BAF engages the nucleosome upside down compared with BAF-OS$^{+6.0}$ class 1 in (B); however, the direction of remodeling in respect to OCT4–SOX2 remains unchanged (remodeling of the nucleosome toward the TFs). The direction of DNA translocation is indicated by the white arrow in the schematic representation.

modules together were refined to 4.0 Å (Figure S7; Table 1) (see STAR Methods). The local resolutions ranged from 3 to 6 Å for the BASE module, nucleosome, and HSA helix, and 8 to 20 Å for the ARP module, the ATPase, and the TFs (Figures S7B and S7C). The resultant composite map (Figure 5A) allowed building of an atomic model for the ternary complex, detailing the structural rearrangements of the BAF remodeler that enabled the accommodation of OCT4–SOX2 close to the EXIT site (Figure 5B). Comparison of this model to previously determined TF-free BAF-NCP structures[40,41] found that the ARP module (comprising its subunits BAF53 [ACTL6A] and β-ACTIN [ACTB]) and the HSA alpha-helix of the BRG1/BRM ATPase underwent the most significant conformational changes (Figures 5C–5E). In particular, the HSA α-helix translated 30 Å toward the nucleosome dyad. This conformational change resolves the expected clash between OCT4–SOX2 and the remodeler, accommodating the OCT4–SOX2 footprint at the EXIT site (Figures 5C–5E; Video S5). As an integral element of the SWI/SNF architecture, the ARP-HSA helix module bridges the ATPase catalytic domain and the BASE module. Accordingly, changes in the ARP-HSA helix directly affect the ATPase position. The two ATPase lobes are displaced from their canonical sites. Lobe 1 (the N-terminal lobe) is in proximity to SHL + 4.5 adjacent to SOX2 and is not engaging in any discernible DNA contacts (Figures 5A, 5B, and 5D). Lobe 2 (the C-terminal lobe) is located adjacent to SHL − 3.5 yet is shifted toward the histone surface rather than sitting on top of nucleosomal DNA (Figures 5A and 5D). A similar structural organization with fully separated ATPase lobes and movement of lobe 2 toward the histone face has been recently described for the related SNF2-type ATPase SNF2H.[68] The conformational changes in the ARP-HSA module in the presence of OCT4–SOX2 at SHL + 6.0 also affect the remodeler BASE module. Compared with the published TF-free BAF-NCP structures,[40,41] the HSA helix in BAF-OS$^{+6.0}$ class 2 undergoes a 55°–75° rotation relative to ATPase lobe 1, which puts the ATPase, the HSA helix, and the BAF250 ARM region of the BASE module roughly co-planar on the same longitudinal axis (Figure S8A). This results in a ~35–45 Å lateral shift of the BAF250 ARM region and of the closely associated subunits (the coiled-coil domains of BAF155/BAF170 (SMARCC1/2), BAF57 (SMARCE1), the SWIB domain of BAF60, and the winged helix domain of BAF47) (Figure S8B). The extensive conformational changes of the remodeler are contrasted by only minor changes in the interaction between OCT4–SOX2 and the nucleosome. The overall structure of nucleosome-bound OCT4–SOX2 in BAF-OS$^{+6.0}$ class 2 again strongly resembles that observed in the absence of the remodeler[8] (Figure S8C).

Together, our structural analysis reveals that BAF can engage the SHL + 6.0 nucleosome in two distinct orientations. Depending on the mode of engagement, OCT4–SOX2 is located either at the ENTRY site (class 1), expected to be remodeled onto the nucleosome, or at the EXIT site (class 2), poised to be

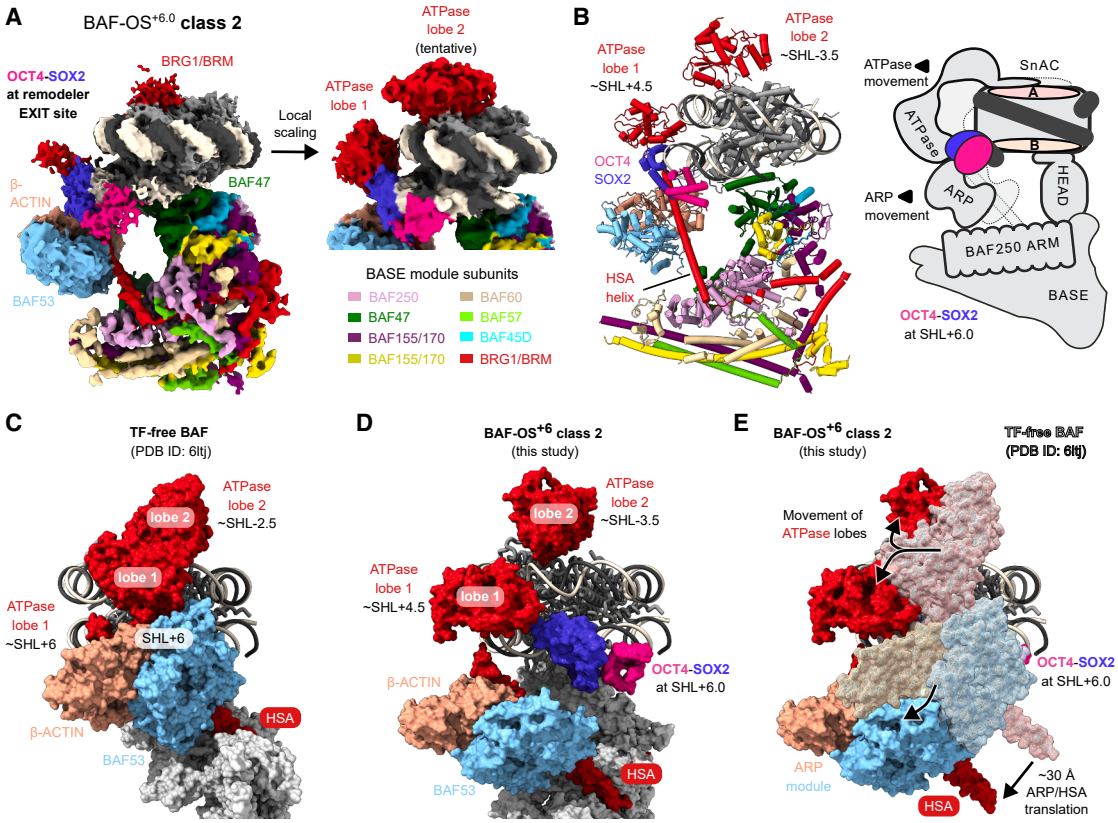

Figure 5. BAF accommodates TFs at the EXIT site in BAF-OS$^{+6.0}$ class 2

(A) BAF-OS$^{+6.0}$ class 2 composite cryo-EM map, colored by subunit. Left: the higher threshold map shows the features of the BASE module and the relative fading out of the ATPase due to conformational flexibility, induced by the displacement. Right: the same map at a lower threshold, upon local amplitude scaling, reveals the density for the ATPase lobes.

(B) Left: structural model BAF-OS$^{+6.0}$ class 2 colored by subunit. Right: graphical representation highlighting the structural rearrangements of BAF to enable the accommodation of OCT4–SOX2 at the EXIT site. ARM, armadillo repeats domain.

(C) Close-up view on the ATPase-ARP region for the published BAF-NCP structure in the absence of TFs (PBD: 6ltj).[40] The ATPase catalytic lobes contact nucleosomal DNA around SHL − 2.5 (lobe 2) and SHL + 6 (lobe 1), while the ARP module is positioned near nucleosomal DNA around SHL + 6.

(D) Close-up view on the ATPase-ARP region for BAF-OS$^{+6.0}$ class 2. A rotational movement of the ARP module and HSA helix of the ATPase by ~30 Å enables the accommodation of OCT4–SOX2 at SHL + 6.0. As a result, ATPase lobe 1 shifts toward SHL + 4.5, while lobe 2 relocates toward the histone face, approaching nucleosomal DNA near SHL − 3.5.

(E) Superposition of the ATPase-ARP-HSA regions of BAF-OS$^{+6.0}$ class 2 (solid surface) with those from the published BAF-NCP structure in the absence of TFs (PBD: 6ltj; pale mesh surface).[40] The arrows highlight the rotational movement of the ARP-HSA module in BAF-OS$^{+6.0}$ class 2 and the subsequent displacement of the ATPase lobes. The structures were aligned to the nucleosome of BAF-OS$^{+6.0}$ class 2 (alignment of chains A–D of PDB: 6ltj with chains A–D of BAF-OS$^{+6.0}$ class 2).

remodeled away from the nucleosome. When OCT4–SOX2 is accommodated at the EXIT site, the ATPase catalytic domain in our AMP-PNP-bound structural snapshot adopts a non-DNA-engaged conformation, reminiscent of an inactive remodeler state. This exact conformation, however, is not strictly dependent on the TFs, as it has been previously observed as part of the Snf2H ATPase cycle[68] and therefore does not necessarily reflect an allosterically inhibited remodeler state. Accordingly, restriction enzyme-based remodeling assays demonstrate that BAF remains fully active in the presence of OCT4–SOX2 at the EXIT site, driving nucleosome movement away from the TFs. Reconciling the structural and functional data, we cannot at present distinguish whether BAF remains competent to remodel EXIT site-bound TFs in a conformational state not captured in our structure, or whether BAF instead translocates TF/nucleosome substrates during transient TF dissociation within their normal binding equilibrium. On the other hand, when BAF initially engages TF-bound nucleosomes in an orientation that places the TFs at the ENTRY site, remodeling is likely to cause TF dissociation due to steric clashes in a subset of encounters. Alternatively, the TFs may induce a reorientation of the remodeler on the nucleosome, thereby changing the translocation direction, a behavior frequently observed in single-molecule remodeling experiments performed in the absence of TFs. Such an orientation switch would again place the TFs at the EXIT site, providing an opportunity for BAF to translocate nucleosomes away from the TFs, as observed for a subset of nucleosomes in restriction-based assays.

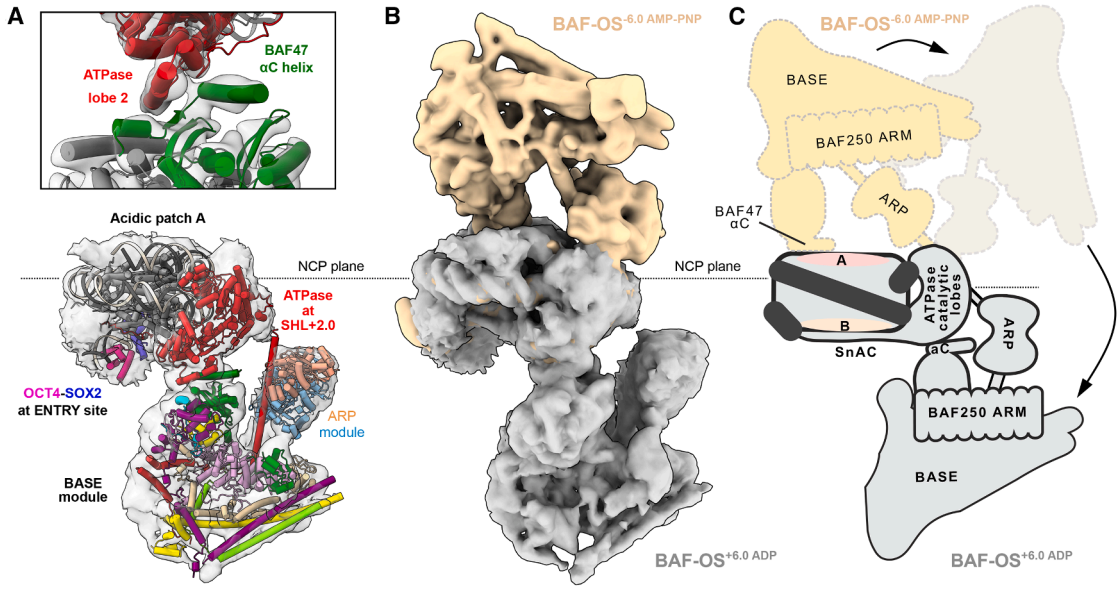

Figure 6. BAF releases a key histone interaction in an ADP-bound state

The structures and graphical representations are aligned relative to the nucleosome (NCP plane), illustrating the conformational changes observed in the BAF-OS$^{+6.0\ ADP}$ class 3 structure.

(A) Upper panel: focused view of the newly formed interface between BAF47 and ATPase lobe 2. Overlay of BAF-OS$^{+6.0\ ADP}$ class 3 cryo-EM map (gray) and model (colored by subunit). Lower panel: overlay of BAF-OS$^{+6.0\ ADP}$ class 3 cryo-EM map (gray) and model (colored by subunit), illustrating how BAF47 released from acidic patch A and relocated to ATPase lobe 2. The ATPase catalytic lobes remain stably engaged with nucleosomal DNA at SHL + 2.0, while OCT4–SOX2 is positioned at the ENTRY site.

(B) Overlay of BAF-OS$^{-6.0\ AMP-PNP}$ cryo-EM map (orange) with BAF-OS$^{+6.0\ ADP}$ class 3 cryo-EM map (gray), highlighting the structural rearrangement of the BASE and ARP module to the opposite face of the nucleosome.

(C) Graphical representation illustrating the conformational rearrangements of BAF as it transitions from a canonical nucleosome engagement state (orange) to the ADP-bound state (gray). The transparent conformation (orange-gray) represents a proposed intermediate, in which BAF47 disengaged from acidic patch A and relocated to the opposite side of the nucleosome. ARM, armadillo repeats domain.

BAF47 can release from the acidic patch

The conformational states of the SWI/SNF ATPase throughout the ATP cycle are well characterized,[46,55–58,69] yet it is not well known whether and how these structural changes impact different parts of the fully assembled complex. When preparing a BAF-OS$^{+6.0}$ cryo-EM sample in the presence of ADP, we observed the two previously described conformational states of BAF (class 1 and class 2), as well as a third distinct class in 2D and 3D reconstructions (class 3, Figure S9). There, the BASE module has lost its key interaction with acidic patch A of the nucleosome, previously mediated by the BAF47 αC-helix (Figures 6A, 6B, and 6C). Consequently, the BASE module repositioned to the opposite side of the nucleosome, where its HEAD submodule established a new contact with the ATPase C-terminal catalytic lobe (lobe 2). The ATPase catalytic domain can be found tightly engaged with nucleosomal DNA around SHL + 2.0 and consistent with previous structures of ADP-bound SNF2 ATPases[56–58,70] induces a DNA bulge around its binding site (Figures S10A and S10C). Additionally, the C-terminal SnAC domain of the ATPase remains bound to acidic patch B of the nucleosome. In this previously uncharacterized BAF conformation, density for OCT4–SOX2 can be primarily found at the ENTRY site of the remodeler-nucleosome complex (Figures 6A and S10B). The structure was solved at an overall resolution of 4.6 Å, with local resolutions ranging from 4 to 5 Å for the nucleosome, the ATPase, and the contact between the HEAD submodule and the ATPase, and 6.5 Å for the BASE module (Figure S9; Table 1). The cryo-EM map allowed building an atomic model, detailing the interaction interface formed by the HEAD submodule of the BASE and lobe 2 of the ATPase (Figure 6A). In class 3, the ATPase catalytic domain is better resolved than in class 1 and class 2 conformations bound to AMP-PNP (Figure S10A). It engages the BASE module via two helices previously assigned to the SnAC domain[55,69] but which are structurally part of the ATPase lobe 2, located immediately after Brace helices I and II. The interaction on the BASE module side is mediated exclusively by BAF47 as part of the HEAD submodule, with the interface consisting of the BAF47 RPT2 domain, the αC-helix, and a newly formed beta-sheet bridging the two domains (Figure 6A).

Further expansion of the 2D classes for the AMP-PNP-containing samples for BAF-OS$^{+6.0}$ and BAF-OS$^{-6.0}$ revealed that the class 3 conformation is present in all datasets collected (Figure S11). Using a low-pass filtered map of the structure obtained from the ADP datasets as input for heterogeneous refinement, we could further separate, enrich, and individually reconstruct the class 3 conformation in BAF-OS$^{+6.0}$ and BAF-OS$^{-6.0}$ AMP-PNP-containing samples (Figures S11C–S11G). Although 3D reconstruction was possible, resolution was

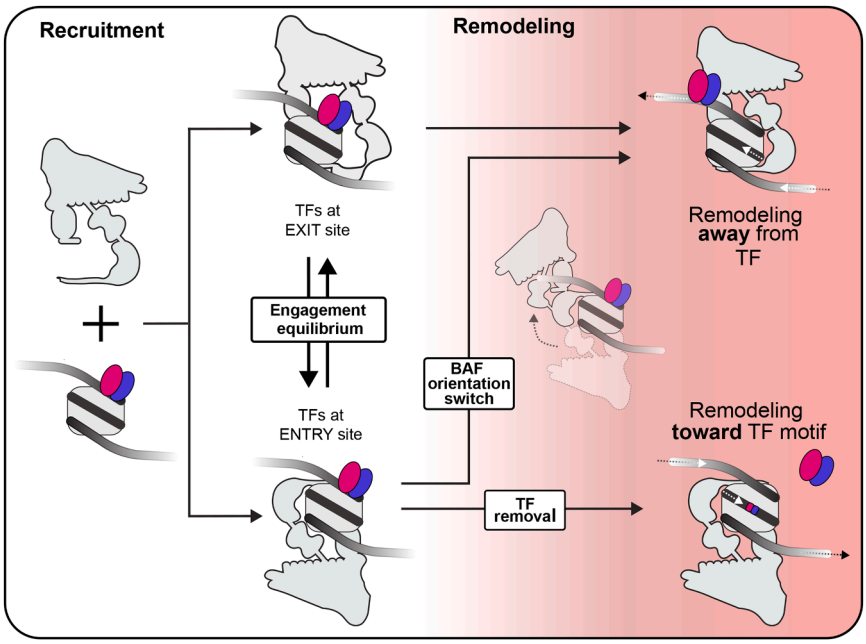

Figure 7. Model figure illustrating the interplay between BAF and OCT4–SOX2-bound nucleosomes

BAF can engage a TF-bound nucleosome in two orientations. While TFs at the ENTRY site do not structurally interfere with BAF, the remodeler undergoes conformational rearrangements to accommodate TFs at the EXIT site. TFs at the EXIT site are poised for translocation away from the nucleosome, while at the ENTRY site, OCT4–SOX2 is initially remodeled toward the remodeler. This can result either in TF displacement or, alternatively, in a reversal of BAF orientation on the nucleosome, enabling remodeling away from the TFs.

limited by the low number of particles. In the case of the ADP-containing samples, the ratio between the sum of particles that gave rise to class 1 and class 2 versus particles in class 3 was ~2:1, while in the presence of AMP-PNP, the ratio was ~10:1. The class 3 conformation comprises up to 40% of the ADP-bound particles, arguing that this is a frequent intermediate in the ATP cycle.

The BAF-OS$^{+6.0\ ADP}$ class 3 structure details how BAF can disengage from one of its primary interaction points on the nucleosome while at the same time remaining stably bound to its nucleosome substrate. To achieve a directional switch, as observed in single-molecule assays (Figure 1D) and suggested for TF-bound nucleosomes initially engaged with OCT4–SOX2 at the ENTRY site, BAF must invert all its contact points with the nucleosome (Figure 1G). The release of BAF47 from the acidic patch constitutes a necessary intermediate in directional switching, providing a recurring opportunity for BAF to change its orientation on a nucleosome during the ATP cycle.

DISCUSSION

Pioneering TFs mark gene regulatory regions genome-wide and drive chromatin opening.[71] Many TFs rely on coactivators such as epigenetic modifiers and chromatin remodeling complexes to establish NDRs and activate transcription,[4,11,12] yet the nature of their crosstalk is poorly understood. In this study, we examined how pioneer TF-bound nucleosomes are processed by the BAF chromatin remodeler. When BAF encounters a nucleosome that is pre-engaged with TFs OCT4–SOX2 (with motif positions at SHL ± 6), the remodeler complex can accommodate TFs both at the remodeler DNA ENTRY or EXIT site. At the ENTRY site, OCT4–SOX2 are initially held without structural interference (Figures 3, 4, and 7) yet are expected to eventually collide with the remodeler once further translocated. Accordingly, we observed reduced nucleosome movement toward the TFs motif in the presence of OCT4–SOX2 (Figure 2F), indicating that the translocation of the TFs onto the nucleosome is possible yet disfavored. Restriction enzyme-based remodeling assays further identified an alternative outcome, where OCT4–SOX2 bias BAF-mediated nucleosome movement away from the TFs by inverting the remodeling directionality (Figures 2B–2E). The translocation of a TF onto nucleosome-bound BAF hence has two principal outcomes: removal of the TF (or BAF) from the nucleosome or a switch in the translocation direction (Figure 7). Such directional switching is also observed spontaneously in single-molecule assays in the absence of TFs, where we found the BAF ATPase changing directionality in 41% of observed traces without complete dissociation of BAF from the nucleosome (Figures 1D and 1F). The ability to alternate engagement between the two symmetry-related SHL2 sites has previously been observed for two yeast remodelers: the nucleosome-sliding, single-subunit remodeler Chd1, and the histone dimer-exchanging SWR1.[65,72] Our observation now suggests that this is a more general strategy by which chromatin remodelers can achieve specific remodeling outcomes within a single binding event. Our corresponding BAF structures now identify the BAF47-nucleosome contact as being frequently disengaged in the ATP hydrolysis cycle (up to 40% of particles), providing a rationale for how such a directionality switch can be initiated (Figure 6). Taken together, functionally, we find that moving a TF motif onto a nucleosome can initiate, or at least facilitate, a sequence of events that switches remodeler directionality, which in turn requires the breakage of BAF/nucleosome contacts, including the BAF47-nucleosome interaction.

What are the implications of this model for TF deposition and maintenance in open chromatin? BAF colocalizes with diverse TFs through protein-protein interactions such as AP-1, C/EBPα, GR, PU.1, OCT4, etc.[15,23,24,26,73] (reviewed in Ho et al.[27]). These interactions may simply help recruit the remodeler to nucleosomes pre-loaded with interacting TFs. When placed at the EXIT site, the TFs will be translocated away from the remodeler, generating open sites unobstructed by

chromatin. When placed at the ENTRY site, the possibilities include TF removal or inversion of directionality, with the latter also rendering the TF motif nucleosome-depleted and accessible (Figure 7; Video S6). The directional remodeling response, as well as the ability to attenuate nucleosome movement toward the TFs binding site as we observed for OCT4–SOX2 (Figure 2), are expected to be exacerbated by arrays of TFs, found for example in super enhancers whose function particularly depends on BAF.[19] Multiple TFs are expected to act cooperatively, such that with each successive TF molecule encountered by BAF, the probability of nucleosome movement onto the TF array decreases exponentially. These enzymatic properties are in line with the genome-wide role for BAF in helping TF access sites through a continuous cycle of chromatin remodeling coupled to TF association/dissociation.

Limitations of this study

We find the BAF chromatin remodeling complex frequently changing the direction of remodeling while remaining nucleosome-associated. We further provide an ADP-bound BAF structure consistent with an intermediate conformation during such a switch of remodeler orientation. Moreover, we find a strong correlation between the presence of the pioneer TFs OCT4–SOX2 and a change in the remodeling direction for a subset of nucleosomes. While we infer from these data that the collision between the TF and BAF likely triggers a change in directionality, we do not directly observe all required intermediates and hence cannot fully exclude that other mechanisms, such as transient dissociation of BAF or displacement of the TFs, at least in part, contribute to the observed change in directionality.

RESOURCE AVAILABILITY

Lead contact

Further information and requests for resources and reagents should be directed to and will be fulfilled by the lead contact, Nicolas H. Thomä (nicolas.thoma@epfl.ch).

Materials availability

Materials are available upon request from Nicolas H. Thomä and with a materials transfer agreement with EPFL.

Data and code availability

- The electron microscopy (EM) density maps have been deposited in the Electronic Microscopy Data Bank (EMD: 54030, EMD: 54078, EMD: 54056, and EMD: 54077). Atomic models were deposited at the RCSB Protein Data Bank (PDB: 9RL4, PDB: 9RN2, PDB: 9RMC, and PDB: 9RN1). EM density maps and atomic models are publicly available as of the date of publication.
- This paper does not report original code.
- Any additional information required to reanalyze the data reported in this paper is available from the lead contact upon request.

ACKNOWLEDGMENTS

We thank D. Hess, V. Iesmantavicius, and J. Seebacher (FMI Proteomics and Protein Analysis Facility) for mass spectrometry support; S. Smallwood, K. Shimada, D. Klein, and M. Schütz-Stoffregen for technical assistance; J. Côté and C. Lachance for critical discussions; and members of the Thomä lab for helpful feedback. Support for this work was provided to N.H.T. by the European Research Council under the European Union's Horizon 2020 research program (NucEM, no. 884331), the Novartis Research Foundation, the Swiss National Science Foundation (SNF 31003A_179541, 310030_214852, and Sinergia CRSII5_186230), and the Swiss Cancer Research (KFS-4980-02-2020 and KFS-5933-08-2023). S.D. was supported by the European Research Council (DONUTS, no. 101092623), the Knut and Alice Wallenberg Foundation (2024.0012), the Cancerfonden (25 4453 Pj), and the Swedish Research Council (VR 03255). A.K.M. was supported by a Human Frontier Science Program Long-Term Fellowship, and L.V. was supported by an EMBO fellowship (ALTF 549-2021).

AUTHOR CONTRIBUTIONS

Conceptualization: J.W., L.V., D.D., S.C., A.S., G.R.P., A.K.M., S.D., and N.H.T.; methodology: J.W., L.V., D.D., S.C., A.S., G.K., S.D., and N.H.T.; investigation: J.W., L.V., D.D., S.C., A.S., G.K., G.R.P., K.B., A.K.M., L.K., E.H.-P., M.H., U.P.K., S.M., R.S.G., and M.B.S.; visualization: J.W., L.V., D.D., S.C., and N.H.T.; funding acquisition: L.V., S.D., and N.H.T.; project administration: N.H.T.; supervision: J.W., L.V., D.D., S.C., S.D., and N.H.T.; writing – original draft: J.W., L.V., and N.H.T.; writing – review & editing: J.W., L.V., D.D., S.C., A.S., A.K.M., S.D., and N.H.T.

DECLARATION OF INTERESTS

The authors declare no competing interests.

DECLARATION OF GENERATIVE AI AND AI-ASSISTED TECHNOLOGIES

Portions of this manuscript were edited for clarity and conciseness using OpenAI's ChatGPT. After using this tool or service, the authors reviewed and edited the content as needed and take full responsibility for the content of the publication.

STAR★METHODS

Detailed methods are provided in the online version of this paper and include the following:

- KEY RESOURCES TABLE
- EXPERIMENTAL MODEL AND STUDY PARTICIPANT DETAILS
  - Mammalian cell culture conditions
  - Bacterial culture conditions
  - Insect cell culture conditions
- METHOD DETAILS
  - Protein expression and purification
  - Nucleosome assembly and purification
- QUANTIFICATION AND STATISTICAL ANALYSIS
  - Statistical analysis of restriction enzyme-based remodeling assays
  - Statistical analysis of ensemble FRET-based remodeling experiments

SUPPLEMENTAL INFORMATION

Supplemental information can be found online at https://doi.org/10.1016/j.molcel.2026.01.021.

Received: June 13, 2025
Revised: November 17, 2025
Accepted: January 14, 2026
Published: February 11, 2026

REFERENCES

1. McGinty, R.K., and Tan, S. (2021). Principles of nucleosome recognition by chromatin factors and enzymes. Curr. Opin. Struct. Biol. *71*, 16–26. https://doi.org/10.1016/j.sbi.2021.05.006.

2. Zhou, K., Gaullier, G., and Luger, K. (2019). Nucleosome structure and dynamics are coming of age. Nat. Struct. Mol. Biol. *26*, 3–13. https://doi.org/10.1038/s41594-018-0166-x.

3. Zhu, F., Farnung, L., Kaasinen, E., Sahu, B., Yin, Y., Wei, B., Dodonova, S.O., Nitta, K.R., Morgunova, E., Taipale, M., et al. (2018). The interaction landscape between transcription factors and the nucleosome. Nature *562*, 76–81. https://doi.org/10.1038/s41586-018-0549-5.

4. Carminati, M., Vecchia, L., Stoos, L., and Thomä, N.H. (2024). Pioneer factors: Emerging rules of engagement for transcription factors on chromatinized DNA. Curr. Opin. Struct. Biol. *88*, 102875. https://doi.org/10.1016/j.sbi.2024.102875.

5. Grand, R.S., Pregnolato, M., Baumgartner, L., Hoerner, L., Burger, L., and Schübeler, D. (2024). Genome access is transcription factor-specific and defined by nucleosome position. Mol. Cell *84*, 3455–3468.e6. https://doi.org/10.1016/j.molcel.2024.08.009.

6. Sinha, K.K., Bilokapic, S., Du, Y., Malik, D., and Halic, M. (2023). Histone modifications regulate pioneer transcription factor cooperativity. Nature *619*, 378–384. https://doi.org/10.1038/s41586-023-06112-6.

7. Guan, R., Lian, T., Zhou, B.R., Wheeler, D., and Bai, Y. (2023). Structural mechanism of LIN28B nucleosome targeting by OCT4. Mol. Cell *83*, 1970–1982.e6. https://doi.org/10.1016/j.molcel.2023.05.030.

8. Michael, A.K., Grand, R.S., Isbel, L., Cavadini, S., Kozicka, Z., Kempf, G., Bunker, R.D., Schenk, A.D., Graff-Meyer, A., Pathare, G.R., et al. (2020). Mechanisms of OCT4-SOX2 motif readout on nucleosomes. Science *368*, 1460–1465. https://doi.org/10.1126/science.abb0074.

9. ENCODE; Project Consortium, Moore, J.E., Purcaro, M.J., Pratt, H.E., Epstein, C.B., Shoresh, N., Adrian, J., Kawli, T., Davis, C.A., Dobin, A., et al. (2020). Expanded encyclopaedias of DNA elements in the human and mouse genomes. Nature *583*, 699–710. https://doi.org/10.1038/s41586-020-2493-4.

10. ENCODE; Project Consortium, Snyder, M.P., Gingeras, T.R., Moore, J.E., Weng, Z., Gerstein, M.B., Ren, B., Hardison, R.C., Stamatoyannopoulos, J.A., Graveley, B.R., et al. (2020). Perspectives on ENCODE. Nature *583*, 693–698. https://doi.org/10.1038/s41586-020-2449-8.

11. Isbel, L., Grand, R.S., and Schübeler, D. (2022). Generating specificity in genome regulation through transcription factor sensitivity to chromatin. Nat. Rev. Genet. *23*, 728–740. https://doi.org/10.1038/s41576-022-00512-6.

12. Ahmad, K., Brahma, S., and Henikoff, S. (2024). Epigenetic pioneering by SWI/SNF family remodelers. Mol. Cell *84*, 194–201. https://doi.org/10.1016/j.molcel.2023.10.045.

13. Lian, T., Guan, R., Zhou, B.R., and Bai, Y. (2024). Structural mechanism of synergistic targeting of the CX3CR1 nucleosome by PU.1 and C/EBPalpha. Nat. Struct. Mol. Biol. *31*, 633–643. https://doi.org/10.1038/s41594-023-01189-z.

14. Minderjahn, J., Schmidt, A., Fuchs, A., Schill, R., Raithel, J., Babina, M., Schmidl, C., Gebhard, C., Schmidhofer, S., Mendes, K., et al. (2020). Mechanisms governing the pioneering and redistribution capabilities of the non-classical pioneer PU.1. Nat. Commun. *11*, 402. https://doi.org/10.1038/s41467-019-13960-2.

15. Frederick, M.A., Williamson, K.E., Fernandez Garcia, M., Ferretti, M.B., McCarthy, R.L., Donahue, G., Luzete Monteiro, E., Takenaka, N., Reynaga, J., Kadoch, C., et al. (2023). A pioneer factor locally opens compacted chromatin to enable targeted ATP-dependent nucleosome remodeling. Nat. Struct. Mol. Biol. *30*, 31–37. https://doi.org/10.1038/s41594-022-00886-5.

16. Chambers, C., Cermakova, K., Chan, Y.S., Kurtz, K., Wohlan, K., Lewis, A.H., Wang, C., Pham, A., Dejmek, M., Sala, M., et al. (2023). SWI/SNF Blockade Disrupts PU.1-Directed Enhancer Programs in Normal Hematopoietic Cells and Acute Myeloid Leukemia. Cancer Res. *83*, 983–996. https://doi.org/10.1158/0008-5472.CAN-22-2129.

17. King, H.W., and Klose, R.J. (2017). The pioneer factor OCT4 requires the chromatin remodeller BRG1 to support gene regulatory element function in mouse embryonic stem cells. eLife *6*, e22631. https://doi.org/10.7554/eLife.22631.

18. Mivelaz, M., Cao, A.M., Kubik, S., Zencir, S., Hovius, R., Boichenko, I., Stachowicz, A.M., Kurat, C.F., Shore, D., and Fierz, B. (2020). Chromatin Fiber Invasion and Nucleosome Displacement by the Rap1 Transcription Factor. Mol. Cell *77*, 488–500.e9. https://doi.org/10.1016/j.molcel.2019.10.025.

19. Schick, S., Grosche, S., Kohl, K.E., Drpic, D., Jaeger, M.G., Marella, N.C., Imrichova, H., Lin, J.G., Hofstätter, G., Schuster, M., et al. (2021). Acute BAF perturbation causes immediate changes in chromatin accessibility. Nat. Genet. *53*, 269–278. https://doi.org/10.1038/s41588-021-00777-3.

20. Friman, E.T., Deluz, C., Meireles-Filho, A.C., Govindan, S., Gardeux, V., Deplancke, B., and Suter, D.M. (2019). Dynamic regulation of chromatin accessibility by pluripotency transcription factors across the cell cycle. eLife *8*, e50087. https://doi.org/10.7554/eLife.50087.

21. Yoshinaga, S.K., Peterson, C.L., Herskowitz, I., and Yamamoto, K.R. (1992). Roles of SWI1, SWI2, and SWI3 proteins for transcriptional enhancement by steroid receptors. Science *258*, 1598–1604. https://doi.org/10.1126/science.1360703.

22. Yudkovsky, N., Logie, C., Hahn, S., and Peterson, C.L. (1999). Recruitment of the SWI/SNF chromatin remodeling complex by transcriptional activators. Genes Dev. *13*, 2369–2374. https://doi.org/10.1101/gad.13.18.2369.

23. Wolf, B.K., Zhao, Y., McCray, A., Hawk, W.H., Deary, L.T., Sugiarto, N.W., LaCroix, I.S., Gerber, S.A., Cheng, C., and Wang, X. (2023). Cooperation of chromatin remodeling SWI/SNF complex and pioneer factor AP-1 shapes 3D enhancer landscapes. Nat. Struct. Mol. Biol. *30*, 10–21. https://doi.org/10.1038/s41594-022-00880-x.

24. Esch, D., Vahokoski, J., Groves, M.R., Pogenberg, V., Cojocaru, V., Vom Bruch, H., Han, D., Drexler, H.C.A., Araúzo-Bravo, M.J., Ng, C.K.L., et al. (2013). A unique Oct4 interface is crucial for reprogramming to pluripotency. Nat. Cell Biol. *15*, 295–301. https://doi.org/10.1038/ncb2680.

25. Gouhier, A., Dumoulin-Gagnon, J., Lapointe-Roberge, V., Harris, J., Balsalobre, A., and Drouin, J. (2024). Pioneer factor Pax7 initiates two-step cell-cycle-dependent chromatin opening. Nat. Struct. Mol. Biol. *31*, 92–101. https://doi.org/10.1038/s41594-023-01152-y.

26. Prekovic, S., Schuurman, K., Mayayo-Peralta, I., Manjón, A.G., Buijs, M., Yavuz, S., Wellenstein, M.D., Barrera, A., Monkhorst, K., Huber, A., et al. (2021). Glucocorticoid receptor triggers a reversible drug-tolerant dormancy state with acquired therapeutic vulnerabilities in lung cancer. Nat. Commun. *12*, 4360. https://doi.org/10.1038/s41467-021-24537-3.

27. Ho, P.J., Lloyd, S.M., and Bao, X. (2019). Unwinding chromatin at the right places: how BAF is targeted to specific genomic locations during development. Development *146*, dev178780. https://doi.org/10.1242/dev.178780.

28. Iurlaro, M., Stadler, M.B., Masoni, F., Jagani, Z., Galli, G.G., and Schübeler, D. (2021). Mammalian SWI/SNF continuously restores local accessibility to chromatin. Nat. Genet. *53*, 279–287. https://doi.org/10.1038/s41588-020-00768-w.

29. Kim, J.M., Visanpattanasin, P., Jou, V., Liu, S., Tang, X., Zheng, Q., Li, K.Y., Snedeker, J., Lavis, L.D., Lionnet, T., et al. (2021). Single-molecule imaging of chromatin remodelers reveals role of ATPase in promoting fast kinetics of target search and dissociation from chromatin. eLife *10*, e69387. https://doi.org/10.7554/eLife.69387.

30. Hager, G.L., McNally, J.G., and Misteli, T. (2009). Transcription dynamics. Mol. Cell *35*, 741–753. https://doi.org/10.1016/j.molcel.2009.09.005.

31. Li, M., Hada, A., Sen, P., Olufemi, L., Hall, M.A., Smith, B.Y., Forth, S., McKnight, J.N., Patel, A., Bowman, G.D., et al. (2015). Dynamic regulation of transcription factors by nucleosome remodeling. eLife *4*, e06249. https://doi.org/10.7554/eLife.06249.

32. Morgunova, E., and Taipale, J. (2021). Structural insights into the interaction between transcription factors and the nucleosome. Curr. Opin. Struct. Biol. *71*, 171–179. https://doi.org/10.1016/j.sbi.2021.06.016.

33. Clapier, C.R., and Cairns, B.R. (2009). The biology of chromatin remodeling complexes. Annu. Rev. Biochem. *78*, 273–304. https://doi.org/10.1146/annurev.biochem.77.062706.153223.

34. Clapier, C.R., Iwasa, J., Cairns, B.R., and Peterson, C.L. (2017). Mechanisms of action and regulation of ATP-dependent chromatin-remodelling complexes. Nat. Rev. Mol. Cell Biol. *18*, 407–422. https://doi.org/10.1038/nrm.2017.26.

35. Narlikar, G.J., Sundaramoorthy, R., and Owen-Hughes, T. (2013). Mechanisms and functions of ATP-dependent chromatin-remodeling enzymes. Cell *154*, 490–503. https://doi.org/10.1016/j.cell.2013.07.011.

36. Becker, P.B., and Workman, J.L. (2013). Nucleosome remodeling and epigenetics. Cold Spring Harb. Perspect. Biol. *5*, a017905. https://doi.org/10.1101/cshperspect.a017905.

37. Gangaraju, V.K., and Bartholomew, B. (2007). Mechanisms of ATP dependent chromatin remodeling. Mutat. Res. *618*, 3–17. https://doi.org/10.1016/j.mrfmmm.2006.08.015.

38. Mashtalir, N., D'Avino, A.R., Michel, B.C., Luo, J., Pan, J., Otto, J.E., Zullow, H.J., McKenzie, Z.M., Kubiak, R.L., St Pierre, R., et al. (2018). Modular Organization and Assembly of SWI/SNF Family Chromatin Remodeling Complexes. Cell *175*, 1272–1288.e20. https://doi.org/10.1016/j.cell.2018.09.032.

39. Centore, R.C., Sandoval, G.J., Soares, L.M.M., Kadoch, C., and Chan, H.M. (2020). Mammalian SWI/SNF Chromatin Remodeling Complexes: Emerging Mechanisms and Therapeutic Strategies. Trends Genet. *36*, 936–950. https://doi.org/10.1016/j.tig.2020.07.011.

40. He, S., Wu, Z., Tian, Y., Yu, Z., Yu, J., Wang, X., Li, J., Liu, B., and Xu, Y. (2020). Structure of nucleosome-bound human BAF complex. Science *367*, 875–881. https://doi.org/10.1126/science.aaz9761.

41. Mashtalir, N., Suzuki, H., Farrell, D.P., Sankar, A., Luo, J., Filipovski, M., D'Avino, A.R., St Pierre, R., Valencia, A.M., Onikubo, T., et al. (2020). A Structural Model of the Endogenous Human BAF Complex Informs Disease Mechanisms. Cell *183*, 802–817.e24. https://doi.org/10.1016/j.cell.2020.09.051.

42. Patel, A.B., Moore, C.M., Greber, B.J., Luo, J., Zukin, S.A., Ranish, J., and Nogales, E. (2019). Architecture of the chromatin remodeler RSC and insights into its nucleosome engagement. eLife *8*, e54449. https://doi.org/10.7554/eLife.54449.

43. Han, Y., Reyes, A.A., Malik, S., and He, Y. (2020). Cryo-EM structure of SWI/SNF complex bound to a nucleosome. Nature *579*, 452–455. https://doi.org/10.1038/s41586-020-2087-1.

44. Wagner, F.R., Dienemann, C., Wang, H., Stützer, A., Tegunov, D., Urlaub, H., and Cramer, P. (2020). Structure of SWI/SNF chromatin remodeller RSC bound to a nucleosome. Nature *579*, 448–451. https://doi.org/10.1038/s41586-020-2088-0.

45. Ye, Y., Wu, H., Chen, K., Clapier, C.R., Verma, N., Zhang, W., Deng, H., Cairns, B.R., Gao, N., and Chen, Z. (2019). Structure of the RSC complex bound to the nucleosome. Science *366*, 838–843. https://doi.org/10.1126/science.aay0033.

46. Wang, L., Yu, J., Yu, Z., Wang, Q., Li, W., Ren, Y., Chen, Z., He, S., and Xu, Y. (2022). Structure of nucleosome-bound human PBAF complex. Nat. Commun. *13*, 7644. https://doi.org/10.1038/s41467-022-34859-5.

47. Yuan, J., Chen, K., Zhang, W., and Chen, Z. (2022). Structure of human chromatin-remodelling PBAF complex bound to a nucleosome. Nature *605*, 166–171. https://doi.org/10.1038/s41586-022-04658-5.

48. He, Z., Chen, K., Ye, Y., and Chen, Z. (2021). Structure of the SWI/SNF complex bound to the nucleosome and insights into the functional modularity. Cell Discov. *7*, 28. https://doi.org/10.1038/s41421-021-00262-5.

49. Schwanbeck, R., Xiao, H., and Wu, C. (2004). Spatial contacts and nucleosome step movements induced by the NURF chromatin remodeling complex. J. Biol. Chem. *279*, 39933–39941. https://doi.org/10.1074/jbc.M406060200.

50. Saha, A., Wittmeyer, J., and Cairns, B.R. (2005). Chromatin remodeling through directional DNA translocation from an internal nucleosomal site. Nat. Struct. Mol. Biol. *12*, 747–755. https://doi.org/10.1038/nsmb973.

51. Zofall, M., Persinger, J., Kassabov, S.R., and Bartholomew, B. (2006). Chromatin remodeling by ISW2 and SWI/SNF requires DNA translocation inside the nucleosome. Nat. Struct. Mol. Biol. *13*, 339–346. https://doi.org/10.1038/nsmb1071.

52. McKnight, J.N., Jenkins, K.R., Nodelman, I.M., Escobar, T., and Bowman, G.D. (2011). Extranucleosomal DNA binding directs nucleosome sliding by Chd1. Mol. Cell. Biol. *31*, 4746–4759. https://doi.org/10.1128/MCB.05735-11.

53. Dechassa, M.L., Zhang, B., Horowitz-Scherer, R., Persinger, J., Woodcock, C.L., Peterson, C.L., and Bartholomew, B. (2008). Architecture of the SWI/SNF-nucleosome complex. Mol. Cell. Biol. *28*, 6010–6021. https://doi.org/10.1128/MCB.00693-08.

54. Sabantsev, A., Levendosky, R.F., Zhuang, X., Bowman, G.D., and Deindl, S. (2019). Direct observation of coordinated DNA movements on the nucleosome during chromatin remodelling. Nat. Commun. *10*, 1720. https://doi.org/10.1038/s41467-019-09657-1.

55. Liu, X., Li, M., Xia, X., Li, X., and Chen, Z. (2017). Mechanism of chromatin remodelling revealed by the Snf2-nucleosome structure. Nature *544*, 440–445. https://doi.org/10.1038/nature22036.

56. Li, M., Xia, X., Tian, Y., Jia, Q., Liu, X., Lu, Y., Li, M., Li, X., and Chen, Z. (2019). Mechanism of DNA translocation underlying chromatin remodelling by Snf2. Nature *567*, 409–413. https://doi.org/10.1038/s41586-019-1029-2.

57. Malik, D., Deshmukh, A., Bilokapic, S., and Halic, M. (2025). Mechanisms of chromatin remodeling by the human Snf2-type ATPase SNF2H. Cell Res. *35*, 465–468. https://doi.org/10.1038/s41422-025-01103-w.

58. Sia, Y., Pan, H., Chen, K., and Chen, Z. (2025). Structural insights into chromatin remodeling by ISWI during active ATP hydrolysis. Science *388*, eadu5654. https://doi.org/10.1126/science.adu5654.

59. Nodelman, I.M., Folkwein, H.J., Glime, W.S., Armache, J.P., and Bowman, G.D. (2025). A competitive regulatory mechanism of the Chd1 remodeler is integral to distorting nucleosomal DNA. Nat. Struct. Mol. Biol. *32*, 1445–1455. https://doi.org/10.1038/s41594-025-01556-y.

60. Michael, A.K., and Thomä, N.H. (2021). Reading the chromatinized genome. Cell *184*, 3599–3611. https://doi.org/10.1016/j.cell.2021.05.029.

61. Lowary, P.T., and Widom, J. (1998). New DNA sequence rules for high affinity binding to histone octamer and sequence-directed nucleosome positioning. J. Mol. Biol. *276*, 19–42. https://doi.org/10.1006/jmbi.1997.1494.

62. Winger, J., and Bowman, G.D. (2017). The Sequence of Nucleosomal DNA Modulates Sliding by the Chd1 Chromatin Remodeler. J. Mol. Biol. *429*, 808–822. https://doi.org/10.1016/j.jmb.2017.02.002.

63. Deindl, S., Hwang, W.L., Hota, S.K., Blosser, T.R., Prasad, P., Bartholomew, B., and Zhuang, X. (2013). ISWI remodelers slide nucleosomes with coordinated multi-base-pair entry steps and single-base-pair exit steps. Cell *152*, 442–452. https://doi.org/10.1016/j.cell.2012.12.040.

64. Engl, W., Kunstar-Thomas, A., Chen, S., Ng, W.S., Sielaff, H., and Zhao, Z.W. (2024). Single-molecule imaging of SWI/SNF chromatin remodelers reveals bromodomain-mediated and cancer-mutants-specific landscape of multi-modal DNA-binding dynamics. Engl. Nat. Commun. *15*, 7646. https://doi.org/10.1038/s41467-024-52040-y.

65. Qiu, Y., Levendosky, R.F., Chakravarthy, S., Patel, A., Bowman, G.D., and Myong, S. (2017). The Chd1 Chromatin Remodeler Shifts Nucleosomal DNA Bidirectionally as a Monomer. Mol. Cell *68*, 76–88.e6. https://doi.org/10.1016/j.molcel.2017.08.018.

66. Stark, H. (2010). GraFix: stabilization of fragile macromolecular complexes for single particle cryo-EM. Methods Enzymol. *481*, 109–126. https://doi.org/10.1016/S0076-6879(10)81005-5.

67. Punjani, A., and Fleet, D.J. (2023). 3DFlex: determining structure and motion of flexible proteins from cryo-EM. Nat. Methods *20*, 860–870. https://doi.org/10.1038/s41592-023-01853-8.

68. Malik, D., Deshmukh, A., Bilokapic, S., and Halic, M. (2025;35(6):465-468). Mechanisms of chromatin remodeling by the human Snf2-type ATPase SNF2H. Cell Res. https://doi.org/10.1038/s41422-025-01103-w.

69. Xia, X., Liu, X., Li, T., Fang, X., and Chen, Z. (2016). Structure of chromatin remodeler Swi2/Snf2 in the resting state. Nat. Struct. Mol. Biol. *23*, 722–729. https://doi.org/10.1038/nsmb.3259.

70. Winger, J., Nodelman, I.M., Levendosky, R.F., and Bowman, G.D. (2018). A twist defect mechanism for ATP-dependent translocation of nucleosomal DNA. eLife *7*, e34100. https://doi.org/10.7554/eLife.34100.

71. Bulyk, M.L., Drouin, J., Harrison, M.M., Taipale, J., and Zaret, K.S. (2023). Pioneer factors - key regulators of chromatin and gene expression. Nat. Rev. Genet. *24*, 809–815. https://doi.org/10.1038/s41576-023-00648-z.

72. Girvan, P., Jalal, A.S.B., McCormack, E.A., Skehan, M.T., Knight, C.L., Wigley, D.B., and Rueda, D.S. (2024). Nucleosome flipping drives kinetic proofreading and processivity by SWR1. Nature *636*, 251–257. https://doi.org/10.1038/s41586-024-08152-y.

73. Pedersen, T.A., Kowenz-Leutz, E., Leutz, A., and Nerlov, C. (2001). Cooperation between C/EBPalpha TBP/TFIIB and SWI/SNF recruiting domains is required for adipocyte differentiation. Genes Dev. *15*, 3208–3216. https://doi.org/10.1101/gad.209901.

74. Vasudevan, D., Chua, E.Y.D., and Davey, C.A. (2010). Crystal structures of nucleosome core particles containing the '601' strong positioning sequence. J. Mol. Biol. *403*, 1–10. https://doi.org/10.1016/j.jmb.2010.08.039.

75. Elegheert, J., Behiels, E., Bishop, B., Scott, S., Woolley, R.E., Griffiths, S.C., Byrne, E.F.X., Chang, V.T., Stuart, D.I., Jones, E.Y., et al. (2018). Lentiviral transduction of mammalian cells for fast, scalable and high-level production of soluble and membrane proteins. Nat. Protoc. *13*, 2991–3017. https://doi.org/10.1038/s41596-018-0075-9.

76. Schenk, A.D., Cavadini, S., Thomä, N.H., and Genoud, C. (2020). Live Analysis and Reconstruction of Single-Particle Cryo-Electron Microscopy Data with CryoFLARE. J. Chem. Inf. Model. *60*, 2561–2569. https://doi.org/10.1021/acs.jcim.9b01102.

77. Tegunov, D., and Cramer, P. (2019). Real-time cryo-electron microscopy data preprocessing with Warp. Nat. Methods *16*, 1146–1152. https://doi.org/10.1038/s41592-019-0580-y.

78. Scheres, S.H.W. (2012). RELION: implementation of a Bayesian approach to cryo-EM structure determination. J. Struct. Biol. *180*, 519–530. https://doi.org/10.1016/j.jsb.2012.09.006.

79. Punjani, A., Rubinstein, J.L., Fleet, D.J., and Brubaker, M.A. (2017). cryoSPARC: algorithms for rapid unsupervised cryo-EM structure determination. Nat. Methods *14*, 290–296. https://doi.org/10.1038/nmeth.4169.

80. Pettersen, E.F., Goddard, T.D., Huang, C.C., Meng, E.C., Couch, G.S., Croll, T.I., Morris, J.H., and Ferrin, T.E. (2021). UCSF ChimeraX: Structure visualization for researchers, educators, and developers. Protein Sci. *30*, 70–82. https://doi.org/10.1002/pro.3943.

81. Emsley, P., Lohkamp, B., Scott, W.G., and Cowtan, K. (2010). Features and development of Coot. Acta Crystallogr., D *66*, 486–501. https://doi.org/10.1107/S0907444910007493.

82. Croll, T.I. (2018). ISOLDE: a physically realistic environment for model building into low-resolution electron-density maps. Acta Crystallogr. D Struct. Biol. *74*, 519–530. https://doi.org/10.1107/S2059798318002425.

83. Jumper, J., Evans, R., Pritzel, A., Green, T., Figurnov, M., Ronneberger, O., Tunyasuvunakool, K., Bates, R., Žídek, A., Potapenko, A., et al. (2021). Highly accurate protein structure prediction with AlphaFold. Nature *596*, 583–589. https://doi.org/10.1038/s41586-021-03819-2.

84. Afonine, P.V., Poon, B.K., Read, R.J., Sobolev, O.V., Terwilliger, T.C., Urzhumtsev, A., and Adams, P.D. (2018). Real-space refinement in PHENIX for cryo-EM and crystallography. Acta Crystallogr. D Struct. Biol. *74*, 531–544. https://doi.org/10.1107/S2059798318006551.

85. Wang, R.Y.R., Song, Y., Barad, B.A., Cheng, Y., Fraser, J.S., and DiMaio, F. (2016). Automated structure refinement of macromolecular assemblies from cryo-EM maps using Rosetta. eLife *5*, e17219. https://doi.org/10.7554/eLife.17219.

86. Williams, C.J., Headd, J.J., Moriarty, N.W., Prisant, M.G., Videau, L.L., Deis, L.N., Verma, V., Keedy, D.A., Hintze, B.J., Chen, V.B., et al. (2018). MolProbity: More and better reference data for improved all-atom structure validation. Protein Sci. *27*, 293–315. https://doi.org/10.1002/pro.3330.

87. Pettersen, E.F., Goddard, T.D., Huang, C.C., Couch, G.S., Greenblatt, D.M., Meng, E.C., and Ferrin, T.E. (2004). UCSF Chimera–a visualization system for exploratory research and analysis. J. Comput. Chem. *25*, 1605–1612. https://doi.org/10.1002/jcc.20084.

88. Schindelin, J., Arganda-Carreras, I., Frise, E., Kaynig, V., Longair, M., Pietzsch, T., Preibisch, S., Rueden, C., Saalfeld, S., Schmid, B., et al. (2012). Fiji: an open-source platform for biological-image analysis. Nat. Methods *9*, 676–682. https://doi.org/10.1038/nmeth.2019.

89. Edelstein, A.D., Tsuchida, M.A., Amodaj, N., Pinkard, H., Vale, R.D., and Stuurman, N. (2014). Advanced methods of microscope control using μManager software. J. Biol. Methods *1*, e10. https://doi.org/10.14440/jbm.2014.36.

90. Sabantsev, A., Mao, G., Aguirre Rivera, J., Panfilov, M., Arseniev, A., Ho, O., Khodorkovskiy, M., and Deindl, S. (2022). Spatiotemporally controlled generation of NTPs for single-molecule studies. Nat. Chem. Biol. *18*, 1144–1151. https://doi.org/10.1038/s41589-022-01100-9.

91. Abdulrahman, W., Uhring, M., Kolb-Cheynel, I., Garnier, J.M., Moras, D., Rochel, N., Busso, D., and Poterszman, A. (2009). A set of baculovirus transfer vectors for screening of affinity tags and parallel expression strategies. Anal. Biochem. *385*, 383–385. https://doi.org/10.1016/j.ab.2008.10.044.

92. Chakraborty, D., Sandate, C.R., Isbel, L., Kempf, G., Weiss, J., Cavadini, S., Kater, L., Seebacher, J., Kozicka, Z., Stoos, L., et al. (2025). Nucleosomes specify co-factor access to p53. Mol. Cell *85*, 2919–2936.e12. https://doi.org/10.1016/j.molcel.2025.06.027.

93. Levendosky, R.F., Sabantsev, A., Deindl, S., and Bowman, G.D. (2016). The Chd1 chromatin remodeler shifts hexasomes unidirectionally. eLife *5*, e21356. https://doi.org/10.7554/eLife.21356.

94. Dyer, P.N., Edayathumangalam, R.S., White, C.L., Bao, Y., Chakravarthy, S., Muthurajan, U.M., and Luger, K. (2004). Reconstitution of nucleosome core particles from recombinant histones and DNA. Methods Enzymol. *375*, 23–44. https://doi.org/10.1016/s0076-6879(03)75002-2.

95. Muthurajan, U., Mattiroli, F., Bergeron, S., Zhou, K., Gu, Y., Chakravarthy, S., Dyer, P., Irving, T., and Luger, K. (2016). In Vitro Chromatin Assembly: Strategies and Quality Control. Methods Enzymol. *573*, 3–41. https://doi.org/10.1016/bs.mie.2016.01.002.

96. Rasnik, I., McKinney, S.A., and Ha, T. (2006). Nonblinking and long-lasting single-molecule fluorescence imaging. Nat. Methods *3*, 891–893. https://doi.org/10.1038/nmeth934.

97. Zivanov, J., Nakane, T., Forsberg, B.O., Kimanius, D., Hagen, W.J., Lindahl, E., and Scheres, S.H. (2018). New tools for automated high-resolution cryo-EM structure determination in RELION-3. eLife *7*, e42166. https://doi.org/10.7554/eLife.42166.

98. Zhang, K. (2016). Gctf: Real-time CTF determination and correction. J. Struct. Biol. *193*, 1–12. https://doi.org/10.1016/j.jsb.2015.11.003.

STAR★METHODS

KEY RESOURCES TABLE

REAGENT or RESOURCE	SOURCE	IDENTIFIER
Bacterial and virus strains		
E. coli BL21-CodonPlus(DE3)-RIL	Agilent	Cat# 230245
NEB Stable Competent *E. coli*	NEB	Cat# C3040H
NEB 5-alpha Competent *E.coli*	NEB	Cat# C2987H
Chemicals, peptides, and recombinant proteins		
Protease inhibitor cocktail	Sigma (Merck)	Cat# S8830
Phusion™ High-Fidelity DNA Polymerase (2U/ul)	Thermo Fisher Scientific	Cat# F530L
Phusion™ HF Buffer Pack	Thermo Fisher Scientific	Cat # F518L
dNTP Mix (10mM each)	Thermo Fisher Scientific	Cat# R0192
Cellfectin™ II	Thermo Fisher Scientific	Cat# 10362100
Desthiobiotin	IBA	Cat# 2-1000-005
SYBR GOLD Nucleic acid stain	Invitrogen	Cat# S11494
Biotin	IBA	Cat# 2-1016-005
H2A K119C (*Xenopus laevis*)	The Histone Source, Colorado State University	XH2A_K119C
H2B (*Xenopus laevis*)	The Histone Source, Colorado State University	XH2B
H3 (*Xenopus laevis*)	The Histone Source, Colorado State University	XH3
H4 (*Xenopus laevis*)	The Histone Source, Colorado State University	XH4
T4 DNA Ligase	BioConcept	Cat# M0202L
Acrylamide:bisacrylamide 37.5:1	Thermo Fisher Scientific	Cat# 330225000
TEMED	Huberlab	Cat# 110-18-9
APS	Huberlab	Cat# 131138.1211
DDM	Anatrace	Cat# D310
AMP-PNP	Sigma	Cat# 10102547001
ADP	Promega	Cat# V6930
ATP	Promega	Cat# V6930
ATP-γ-S	Roche/Sigma	Cat# 11162306001
Glutaraldehyde	Electron Microscopy Sciences	Cat# 16220
Proteinase K	Thermo Fisher Scientific	Cat# EO0491
Acetylated BSA	Promega	Cat# R3961
Streptavidin	Invitrogen	Cat# S-888
Trolox	Sigma	Cat# 238813
glucose oxidase	Sigma	Cat# G2133
catalase	Sigma	Cat# C1345
MfeI-HF restriction enzyme 500U	BioConcept	Cat# R3589S
PmlI restriction enzyme 2000U	BioConcept	Cat# R0532S
Cy3-maleimide	Amersham	Cat# PA23031

(*Continued on next page*)

Continued

REAGENT or RESOURCE	SOURCE	IDENTIFIER
Deposited data		
BAF-OS$^{-6.0}$ model	This study	PDB: 9RL4
BAF-OS$^{-6.0}$ map	This study	EMD-54030
BAF-OS$^{+6.0}$ class1 model	This study	PDB: 9RN2
BAF-OS$^{+6.0}$ class1 map	This study	EMD-54078
BAF-OS$^{+6.0}$ class2 model	This study	PDB: 9RMC
BAF-OS$^{+6.0}$ class2 map	This study	EMD-54056
BAF-OS$^{+6.0}$ ADP model	This study	PDB: 9RN1
BAF-OS$^{+6.0}$ ADP map	This study	EMD-54077
OCT4-SOX2-bound nucleosome – SHL+6	Michael et al.[8]	PDB: 6YOV
OCT4-SOX2-bound nucleosome – SHL-6	Michael et al.[8]	PDB: 6T90
Structure of nucleosome-bound human BAF complex	He et al.[40]	PDB: 6LTJ
Motor-nucleosome module of human PBAF-nucleosome complex	Yuan et al.[47]	PDB: 7VDT
Nucleosome Core Particle containing the Widom 601 DNA sequence	Vasudevan et al.[74]	PDB: 3LZ0
Structure of endogenous human BAF complex bound to nucleosome	Mashtalir et al.[41]	PDBDEV_00000056
Experimental models: Organisms/strains		
E.coli BL21-CodonPlus(DE3)-RIL	Agilent	Cat# 230245
Sf9 Insect cells	Thermo Fisher Scientific	Cat# 11496015
High-Five Insect cells	Thermo Fisher Scientific	Cat# B85502
Expi293F™ mammalian cells	Thermo Fisher Scientific	Cat# A14527
Oligonucleotides		
Primers for ensemble FRET remodeling assays, see Table S1	This study	N/A
Primers for single-molecule FRET remodeling assays, see Table S1	This study	N/A
Primers for cryo-EM templates, see Table S1	This study	N/A
Primers for restriction enzyme-based remodeling assays and EMSAs, see Table S1	This study	N/A
Recombinant DNA		
pHR-CMV-TetO2_3C-Twin-Strep_IRES-EmGFP	Elegheert et al.[75]	Addgene Cat# 113884
pHR-CMV-TetO2_3C-Twin-Strep-Dpf2_IRES-EmGFP	This study	N/A
pAC8-STREPII-GFP-OCT4-Sortase-His(6x)	This study	N/A
pAC8-STREPII-SOX2(aa. 37-118)	This study	N/A
pTwist-601-nuclesome-positioning-sequence	Twist Bioscience	N/A
pTwist-OS^{SHL-6} 40bp overhangs	Twist Bioscience	N/A
pTwist-OS^{SHL+6} 40bp overhangs	Twist Bioscience	N/A
pTwist-OS^{SHL-6} RE 40bp overhangs	Twist Bioscience	N/A
pTwist-OS^{SHL+6} RE 40bp overhangs	Twist Bioscience	N/A
Software and algorithms		
FEI EPU v2.7.0	Thermo Fisher Scientific	https://www.thermofisher.com/
CryoFLARE	Schenk et al.[76]	https://www.cryoflare.org/
Warp	Tegunov and Cramer[77]	https://github.com/cramerlab/warp
Relion	Scheres[78]	https://github.com/3dem/relion

(*Continued on next page*)

Continued

REAGENT or RESOURCE	SOURCE	IDENTIFIER
cryoSPARC v3-v4	Punjani et al.[79]	https://cryosparc.com/
3DFlex	Punjani and Fleet[67]	https://cryosparc.com/heterogeneity
ChimeraX	Pettersen et al.[80]	https://www.rbvi.ucsf.edu/chimerax/
Coot	Emsley et al.[81]	https://www2.mrc-lmb.cam.ac.uk/personal/pemsley/coot/
ISOLDE v1.3	Croll[82]	https://isolde.cimr.cam.ac.uk/
AlphaFold v2.3	Jumper et al.[83]	https://github.com/deepmind/alphafold
Phenix v1.20	Afonine et al.[84]	https://phenix-online.org/
Rosetta	Wang et al.[85]	https://www.rosettacommons.org/
Molprobity	Williams et al.[86]	https://github.com/rlabduke/MolProbity
PyMol v2.3.3	Schrodinger, LLC	https://pymol.org/2/
UCSF Chimera	Pettersen et al.[87]	https://www.cgl.ucsf.edu/chimera/
Fiji ImageJ	Schindelin et al.[88]	https://imagej.net/software/fiji/
Micromanager	Edelstein et al.[89]	https://micro-manager.org
MATLAB	Sabantsev et al.[90]	https://www.mathworks.com/products/matlab.html
Other		
Expi293™ Expression Medium	Thermo Fisher Scientific	Cat# A1435101
SF4 Baculo-Express Media	BioConcept	Cat# 900F38
HiLoad Superdex™ 200pg preparative SEC column	Cytiva	Cat# 28989335
POROS™ Heparin	Thermo Fisher Scientific	Cat# 4329435
POROS™ HQ	Thermo Fisher Scientific	Cat# 82077
Mono Q™ 5/50 GL	Cytiva	Cat# 17-5166-01
Superose™ 6 Increase 10/300 GL	Cytiva	Cat# 29091596
STREP-Tactin® Sepharose 50% suspension	IBA	Cat# 2-1201-010
Strep-TactinXT® 4Flow® high-capacity column, 5 mL	IBA	Cat# 2-5028-001
HiTrap™ Q HP 1ml	Cytiva	Cat# 17115301
HisTrap™ HP, 5ml	Cytiva	Cat# 17-5248-02
Repligen Spectra/Por® RC Dialysis Tubing, MWCO: 6–8kDa	Spectrum	Cat # 132665
Amicon Ultra-4 Centrifugal Filter Unit, Ultracel, 30kDa, 4ml	Merck (EMD Millipore)	Cat# UFC803024
Amicon Ultra-15 Centrifugal Filter Unit, Ultracel, 30kDa, 15ml	Merck (EMD Millipore)	Cat# UFC903024
Amicon Ultra-4 Centrifugal Filter Unit, Ultracel, 100kDa, 4ml	Merck (EMD Millipore)	Cat# UFC810008

EXPERIMENTAL MODEL AND STUDY PARTICIPANT DETAILS

Mammalian cell culture conditions

Expi293F™ mammalian cells were grown in Expi293™ expression medium at 37°C in a humidified incubator (80% humidity) with 8% CO_2 and gentle agitation at 120 rpm. Cells were routinely passaged to maintain exponential growth and harvested at a final cell density between $6x10^6$ cells/mL and $8x10^6$ cells/mL. Expi293F™ cells were obtained from Thermo Fisher Scientific and were not independently authenticated by the authors. Cells were routinely tested for mycoplasma contamination.

Bacterial culture conditions

Human histones were expressed in *Escherichia coli* BL21-CodonPlus(DE3)-RIL cells (Agilent). Cells were cultured in LB medium at 37 °C with shaking at 200 rpm. At an optical density at 600 nm (OD_{600}) of 0.6, protein expression was induced by the addition of isopropyl β-D-1-thiogalactopyranoside (IPTG) to a final concentration of 0.5 mM, followed by 4 h of expression at 37 °C.

Insect cell culture conditions

Trichoplusia ni insect cells were maintained at 27°C with shaking at 120 rpm in SF4 Baculo Express Media (BioConcept). For protein expression, cells were infected with recombinant baculovirus encoding OCT4 or SOX2 and cultured for 48 hours prior to harvest.

METHOD DETAILS

Protein expression and purification

OCT4 and SOX2

Full-length human OCT4 (Uniprot ID Q01860, aa. 1-360) was expressed from a previously described pAC-derived expression plasmid encoding an N-terminal StrepII-tag, a N-terminal EGFP-tag, and a C-terminal sortase-6xHis-tag.[8,91] The DNA-binding domain of human SOX2 (Uniprot ID P48431, aa. 37-118) was produced using a pAC-derived expression construct encoding an N-terminal StrepII-tag.[8,91] Protein expression was performed using a baculovirus expression system in *Trichoplusia ni* High Five insect cells which were cultured for 48 hours at 27°C following infection. Cells were harvested and resuspended in lysis buffer containing 50 mM Tris-HCl pH 8.0, 1 M NaCl, 1 mM phenylmethylsulfonyl fluoride (PMSF), 0.5 mM TCEP, and SIGMAFAST™ Protease Inhibitor Cocktail, and lysed by sonication. Clarified lysates were subjected to affinity purification using Strep-Tactin Sepharose (IBA), followed by heparin ion-exchange chromatography and size-exclusion chromatography using a Superdex™ 200 column (Cytiva). Purified proteins were stored in a final buffer containing 20 mM HEPES pH 7.4, 150 mM NaCl, 5% glycerol, and 0.5 mM TCEP. Related protocols have been described previously.[8]

Human BAF

For the expression of human canonical BAF (BAF), a subunit of the complex encoding a C-terminal Twin-Strep tag was stably integrated in the genome of the target cells under the control of a CMV promoter, and the other endogenous subunits of the complex were purified using the tagged subunit as a bait. In detail, wild-type full-length Dpf2/BAF45d (UNIPROT ID Q92785, aa. 1-391) was cloned in the lentiviral transfer plasmid pHR-CMV-TetO2_3C-Twin-Strep_IRES-EmGFP (Addgene plasmid n.113884) and a stable cell line was generated by lentiviral transduction of Expi293™ mammalian cells (Thermo Fisher Scientific), following the methodology outlined in the published protocol describing this lentiviral plasmid suite.[75] Successfully infected cells – expressing GFP from the same mRNA as the transgene under control of an IRES (internal ribosome entry site) – were enriched by FACS (Fluorescence-activated cell sorting). Cells were scaled up in Expi293™ expression medium and harvested when the cell density reached a value between $6x10^6$ cells/mL and $8x10^6$ cells/mL. Nuclear extraction was performed on the basis of the previously published protocol for endogenous cBAF purification,[41] with several modifications. First, cell pellets were resuspended in hypotonic buffer (10 mM HEPES pH 8, 10 mM KCl, 1.5 mM $MgCl_2$, 1 mM DTT, SIGMAFAST™ Protease Inhibitor Cocktail) and homogenized with a Dounce homogenizer at 4°C. The homogenate was then centrifuged for 30 minutes at 4000 xg at 4°C. The packed nuclear volume (pnv) was measured using a graduated tube and the pellet was resuspended in 2 pnv of pre-extraction buffer (20 mM HEPES pH 8, 100 mM KCl, 1.5 mM $MgCl_2$, 0.2 mM EDTA, 0.1% NP-40, 1 mM DTT, SIGMAFAST™ Protease Inhibitor Cocktail). The suspension was centrifuged for 10 minutes at 4000 xg at 4°C. The pellet was resuspended in ½ pnv of low-salt buffer (20 mM HEPES pH 8, 20 mM KCl, 10% glycerol, 1.5 mM $MgCl_2$, 0.2 mM EDTA, 1 mM DTT, SIGMAFAST™ Protease Inhibitor Cocktail); ½ pnv of high-salt buffer (20 mM HEPES pH 8, 1.2 M KCl, 10% glycerol, 1.5 mM $MgCl_2$, 0.2 mM EDTA, 1 mM DTT, SIGMAFAST™ Protease Inhibitor Cocktail) was added dropwise. The solution was incubated for 1 hour at 4°C under rotation and centrifuged in a Ti45 rotor (Beckman Coulter) for 1 hour at 48900 xg. The supernatant was filtered sequentially trough 1.2-, 0.45- and 0.2-mm filters and loaded on a 5 mL Strep-TactinXT® 4Flow® high-capacity column (IBA). The column was washed with wash buffer (20 mM HEPES pH 8, 300 mM KCl, 1.5 mM $MgCl_2$, 0.2 mM EDTA, 1 mM DTT) and the protein was eluted in 20 mM HEPES pH 8, 100 mM KCl, 1.5 mM $MgCl_2$, 0.2 mM EDTA, 1 mM DTT, 50 mM biotin. The protein was further purified by loading the eluate onto an ion-exchange 1 mL Mono Q™ 5/50 GL column (Cytiva) with binding buffer composed of 20 mM HEPES pH 8, 100 mM KCl, 1 mM $MgCl_2$, 1 mM DTT and elution buffer by 20 mM HEPES pH 8, 1 M KCl, 1 mM $MgCl_2$, 1 mM DTT. Finally, peak fractions from the Mono Q were loaded onto a Superose 6 Increase 10/300 GL column (Cytiva) equilibrated in 20 mM HEPES pH 8, 100 mM KCl, 0.5 mM $MgCl_2$, 5% glycerol, 0.5 mM TCEP.

Human histone expression, purification and octamer reconstitution

Human histones were expressed and purified using a previously reported bacterial expression and refolding workflow.[92] Individual histones (H2A, H2B, H3, and H4) were expressed in *Escherichia coli* as N-terminally His_6-tagged proteins, solubilized under denaturing conditions, and purified by Ni^{2+}-affinity chromatography using a HiTrap His column (Cytiva). Eluted histones were buffer-exchanged to remove denaturant prior to proteolytic removal of the His_6-tag by thrombin. Following tag cleavage, histones were further purified by anion-exchange chromatography on a Poros Q column, buffer-exchanged to remove salt and urea, and subsequently lyophilized. Lyophilized histones were mixed at equimolar ratios in denaturing buffer containing 6M Urea and were dialyzed into refolding buffer (20mM Tris-HCl, pH 7.5, 2M KCl, 1mM DTT). The resulting histone complexes were purified by size exclusion chromatography (Superdex™ 200, Cytiva).

Cy3-H2A labeling and purification of labeled H2A-H2B dimer and H3-H4 Tetramer

H2A K119C, H2B, H3 and H4 (*Xenopus laevis*) were purchased from the histone Source Protein Expression and Purification Facility, Colorado State University, Fort Collins, CO. For labeling, one milligram of lyophilized H2A K119C was diluted in unfolding buffer (20 mM Tris-HCl pH 7.0, 7 M guanidine-HCl, 5 mM EDTA, 1.25 mM TCEP) and incubated for 2 h at room temperature in the dark. Cy3-maleimide was dissolved in DMSO and added to the protein at a final concentration of 0.75 mM. After 3 h in the dark at room temperature, the reaction was quenched with a final concentration of 80 mM β-mercaptoethanol. The labeled protein was dialyzed nine times against dialysis buffer (20 mM Tris-HCl pH 7.0, 7 M guanidine-HCl, 1 mM DTT) and then used in H2A/H2B dimer assembly. The labeling efficiency was >70%.

The histone tetramer was refolded by mixing equimolar amounts of H3 and H4 dissolved in the unfolding buffer (20 mM Tris-HCl pH 7.5, 6 M guanidine HCl, 5 mM DTT) and dialyzing the mixture against refolding buffer (10 mM Tris-HCl pH 7.5, 2 M NaCl, 1 mM EDTA, 5 mM 2-mercaptoethanol) three times throughout 20 h. The resulting histone tetramer was concentrated and purified by size exclusion chromatography on a Superdex™ 200 column (Cytiva).

Nucleosome assembly and purification

DNA amplification

The DNA fragments for nucleosome assembly were amplified from template DNA (plasmid or gene block) by PCR in 96-well plates using Phusion polymerase, Phusion HF buffer and primers at a final concentration of 1 μM each. DNA-sequences and oligonucleotides used in this study are listed in Table S1. PCR products were pooled and purified by anion-exchange chromatography on a HiTrap Q HP column (Cytiva) by loading the sample onto the column at a flow rate of 1 mL/min in 50 mM Tris-HCl pH 8.0, 100 mM NaCl, and 0.1 mM EDTA. Elution was performed using a linear gradient to 1 M NaCl over 20 column volumes. Appropriate fractions were identified by native PAGE on a 10% polyacrylamide gel, pooled, and either subjected to ethanol precipitation followed by resuspension in pure water, or buffer-exchanged by dialysis using a 6-8 kDa molecular-weight cut-off membrane into 10 mM Tris-HCl pH 7.5.

Nucleosome assembly for cryo-EM, restriction enzyme-based remodeling assays, and EMSAs

DNA and histone octamer complex were mixed in a 1:1.5 molar ratio in the presence of 2 M KCl. The samples were transferred into 6–8kDa dialysis tubing and placed into high-salt buffer (10 mM Tris-HCl pH 7.5, 2 M KCl, 1 mM EDTA, and 1 mM DTT). The KCl concentration was gradually reduced from 2 M to 0.25 M using a peristaltic pump with 3 L low-salt buffer (10 mM Tris-HCl pH 7.5, 250 mM KCl, 1 mM EDTA, and 1 mM DTT) at 4°C. After dialysis, nucleosomes were incubated at 55°C for 1–2 hours and purified by a Mono Q 5/50 ion exchange gradient (Cytiva). Purified nucleosomes were dialyzed in no-salt buffer (20 mM Tris-HCl pH 7.5, 0.5 mM TCEP) overnight, concentrated using a 30kDa molecular-weight cut-off Amicon concentrator, and stored at 4°C.

Nucleosome assembly for FRET experiments

Oriented nucleosomes for single-molecule FRET experiments were assembled using a hexasome-based assembly strategy adapted from Levendosky et al.[93] The DNA construct comprises the Widom 601 nucleosome positioning sequence, 9 bp of linker on one side, which is 5′-labeled with Cy5 and 78 bp linker on the other side, which is 3′-biotinylated. First, hexasomes were assembled by mixing DNA, H3/H4 tetramer and H2A(K119C-Cy3)/H2B dimer in a 1:1.2:0.5 molar ratio in a high-salt buffer (10 mM Tris-HCl pH 7.5, 2 M NaCl, 1 mM EDTA, 1 mM DTT) and slowly lowering the NaCl concentration by dialysis over the course of 12 hours.[94,95] Hexasomes were purified over a 7% native acrylamide column (60:1 acrylamide:bisacrylamide) using a MiniPrep Cell (BioRad) apparatus. Complete nucleosomes were assembled before the experiment by adding unlabeled H2A/H2B dimer to hexasomes in 1.2-fold molar excess and incubating at 20°C for 20 minutes. This allowed for a controlled incorporation of the labeled H2A(K119C-Cy3)/H2B dimer on the side of the nucleosomes that is closest to the Cy5-labeled DNA end.

Oriented nucleosomes for ensemble FRET experiments were assembled using a hexasome-based assembly and ligation strategy adapted from Dao et al.[95] Hexasomes were first reconstituted by salt gradient dialysis on a truncated version of the Widom 601 positioning sequence (“core”) that is too short to enable nucleosome formation (Figure S2A). Next, a “stem” DNA piece was ligated to the hexasomes (0.8 μM hexasomes, 1.5x excess of the “stem” DNA, T4 DNA ligase, 5.5-hour linear temperature gradient from +4°C to +37°C in 10 mM Tris-HCl pH 7.5, 6 mM MgCl, 1 mM ATP, 1 mM DTT). The reaction was stopped by addition of EDTA to a final concentration of 10 mM. Finally, complete nucleosomes were assembled before the experiment by adding H2A/H2B dimer to hexasomes in 1.25-fold molar excess and incubating at +20°C for 20 minutes.

Ensemble FRET remodeling experiments

Nucleosome ensemble remodeling kinetics were measured by monitoring the Cy5 (under 620 nm and 520 nm excitation) and Cy3 (under 520 nm excitation) fluorescence emission signals of a solution of FRET-labeled nucleosomes using a CLARIOstar (BMG Labtech) multimode microplate reader in 384-well plates (sample volume 20 μL). Ensemble nucleosome remodeling assays were performed with 7.5 nM nucleosomes, 0.5 mM ATP and 2.5 mM ATP-γ-S in remodeling buffer (20 mM Tris-HCl 7.5, 50 mM KCl, 0.25 mM EDTA, 5 mM $MgCl_2$). Where indicated, 750 nM SOX2 and OCT4 were added to the reactions. Samples were incubated for 5 min at +20°C and remodeling was initiated by adding 25 nM BAF. ATP-γ-S was included to slow down the remodeling reaction which otherwise was too fast for reliable observation. Under these experimental conditions, remodeling of a nucleosome template in the absence of TFs results in a moderate decrease in FRET efficiency from ∼0.35 to ∼0.25. The elevated FRET baseline (∼0.2 in conditions with 1mM ATP and no ATP-γ-S) in these ensemble experiments likely stems from a small fraction of unligated nucleosomes, incomplete Cy3 labeling of the histone hexamer used for reconstitution, and free Cy5-labeled DNA in solution.

Single-molecule FRET experiments

Biotinylated FRET-labeled nucleosomes were immobilized on a PEG (poly[ethylene glycol])-coated quartz slide saturated with streptavidin.[63] Cy3 and Cy5 fluorophores were excited with 532 nm Nd:YAG and 638 nm diode lasers, respectively, and fluorescence emissions from Cy3 and Cy5 fluorophores were detected using a custom-built prism-based TIRF microscope. To check the presence of an intact donor fluorophore, the sample was alternately excited with 532 nm and 638 nm lasers during the experiment. Starting FRET histograms for both the +9bp-nucleosome used in single-molecule experiments and the +12bp-nucleosome used in ensemble FRET experiments were recorded using this setup (Figure S2B). Data acquisition was controlled by MicroManager.[89] Data were analyzed using custom scripts in the Fiji distribution of ImageJ,[88] IDL, and MATLAB.[90] Remodeling experiments were carried out

in the imaging buffer containing 40 mM Tris-HCl pH 7.5, 60 mM KCl, 0.32 mM EDTA, 100 μg/mL acetylated BSA (Promega), 10% (v/v) glycerol, 10% (w/v) glucose, supplemented with 2 mM trolox to reduce photoblinking of the dyes,[96] 125 μg/mL streptavidin (Invitrogen) to prevent interactions between the Strep-tag on BAF and streptavidin on the surface, as well as an enzymatic oxygen scavenging system (composed of 800 μg/mL glucose oxidase and 50 μg/mL catalase). To conduct experiments that allow only for a single nucleosome binding event of BAF, surface-immobilized nucleosomes were first incubated with the imaging buffer supplemented with 20 nM BAF and 0.75 mM ATP for 5 min at +20°C, washed with the imaging buffer supplemented with 0.75 mM ATP, and finally remodeling was initiated by injecting the imaging buffer supplemented with 1.5 mM ATP and 3 mM $MgCl_2$. Switching of the remodeling direction was determined by visually inspecting the FRET traces. Traces were scored as showing direction reversal if an initial FRET decrease was followed by a reproducible FRET increase that rose clearly above the noise level of that trace, prior to donor or acceptor bleaching or the end of the observation window (see example traces in Figure S2C and S2D). To avoid ambiguity due to the non-monotonous behavior of the FRET signal as a function of nucleosome position during movement toward the Cy5-labeled DNA end, only traces starting with a FRET decrease (corresponding to the movement away from the Cy5-labeled DNA end) were included in the analysis.

Restriction enzyme-based remodeling assays

20 μL reactions containing 167 nM nucleosome (3′ FAM labeled), 100 nM (0.6X) BAF remodeler complex, 500 nM (3X) of OCT4-SOX2, 1.3 uM competitor DNA, 20U restriction enzyme (MfeI/PmlI), and 1 mM ATP were prepared in 1X assay buffer (20 mM Tris-HCl pH 7.5, 50 mM KCl, 3 mM MgCl2, 0.1 mg/mL BSA, 0.5mM TCEP). For control samples, BAF and OCT4-SOX2 were replaced by SEC buffer (20 mM HEPES pH 7.4, 150 mM NaCl, 5% glycerol, 0.5 mM TCEP), and ATP was exchanged with H_2O. Remodeling reactions were started by the addition of ATP and subsequently incubated for 30 minutes at 30°C. Reactions were stopped by the addition of 2 μL of stop buffer (10X; 100 mM EDTA pH 8, 5% SDS) and samples were chilled on ice for 10 minutes. Finally, proteins were digested with 20 μg Proteinase K (Thermo Fisher Scientific) for 4 hours at 50°C and DNA fragments were separated on a 6% non-denaturing polyacrylamide gel (acrylamide:bisacrylamide: 37.5:1) in 0.5X TGE buffer for 1 hour in the dark (120V, room temperature). Fluorescence signals were analyzed on a Typhoon imager (Typhoon FLA 9500; Cytiva). Marker bands were visualized by subsequent staining with SYBR Gold nucleic acid stain (~10 min, Invitrogen) and re-imaged on the Typhoon Imager.

EMSAs

EMSAs were performed in 20 μL reactions containing 100 nM nucleosomes (3' FAM-labeled), 250 nM OCT4-SOX2, and 100 nM BAF, prepared in 1X binding buffer (20 mM Tris-HCl pH 7.5, 75 mM NaCl, 10 mM KCl, 1 mM $MgCl_2$, 0.1 mg/mL BSA, and 1 mM DTT). For control samples lacking specific components, OCT4-SOX2 and BAF were replaced with SEC buffer (20 mM HEPES pH 7.4, 150 mM NaCl, 5% glycerol, 0.5 mM TCEP). Reactions were incubated at room temperature for 1 hour, then loaded onto a 4% non-denaturing polyacrylamide gel (acrylamide:bisacrylamide = 37.5:1) in 0.5X TGE buffer. Gels were run at 120V for 1 hour at room temperature in the dark. Fluorescence signals were detected using a Typhoon FLA 9500 Imager (Cytiva). Marker bands were visualized by subsequent staining with SYBR Gold nucleic acid stain (~10 min, Invitrogen) and re-imaged on the Typhoon Imager.

BAF-NCP-TFs complex formation and cryo-EM sample preparation

The BAF-NCP-OCT4/SOX2 complexes were formed by mixing the components in a molar ratio of 1:1.5:4.5 (remodeler:nucleosome:TFs). First, OCT4 and SOX2 were added to the nucleosome and incubated for 30 minutes at 4°C. Then, BAF was added, the mixture was supplemented with 1 mM of the non-hydrolysable ATP-analogue adenyl-5'-yl imidodiphosphate (AMP-PNP, Sigma) or ADP (Promega) and incubated for 2 hours at 4°C. The sample was loaded on top of a 4 mL 10-40% sucrose and 0%-0.1% glutaraldehyde gradient following the GraFix protocol[66] (top solution: 20 mM HEPES pH 8, 100 mM KCl, 0.5 mM $MgCl_2$, 0.5 mM TCEP, 10% w/v sucrose; bottom solution: 20 mM HEPES pH 8, 100 mM KCl, 0.5 mM $MgCl_2$, 0.5 mM TCEP, 40% w/v sucrose, 0.1% glutaraldehyde). Gradient ultracentrifugation was carried out at 140000 xg for 14 hours at 4°C using a Beckman SW60Ti rotor. 100 μL fractions were collected from the gradient using a Biocomp Piston Gradient Fractionator™ system and quenched by the addition of 100 mM Tris-HCl pH 7.5. Peak fractions containing the ternary complex were selected by native PAGE stained with SYBR gold (Invitrogen), pooled and dialyzed overnight in buffer containing 20 mM HEPES pH 8, 100 mM KCl, 0.5 mM $MgCl_2$, 0.5 mM TCEP to remove the excess sucrose. The sample was concentrated to approximately 1.5 mg/mL to prepare cryo-EM grids, using Amicon® Ultra centrifugal filters (Millipore) with a molecular-weight cut-off of 100 kDa. For EM grids prepared in presence of detergent, 0.003% w/v DDM (n-Dodecyl-β-D-Maltoside, Anatrace) was added to the sample just before grid freezing, and the final protein concentration was about 2.5 mg/mL. For cryo-EM grid preparation, Quantifoil holey carbon grids (R 1.2/1.3, 200-mesh, Quantifoil Micro Tools) were glow discharged using a GloQube Plus (Quorum Technologies Limited) for 30 seconds, and 3.5-4 μL of sample were applied on the grids. After a 5-second waiting time at 4°C, the grids were subsequently blotted for 3-4 seconds at 100% humidity and plunge-frozen into liquid ethane using a Vitrobot Mark IV (Thermo Fisher Scientific).

Cryo-EM data collection

Data were collected automatically with EPU (Thermo Fisher Scientific) on a Cs-corrected (CEOS GmbH, Heidelberg, Germany) Titan Krios (Thermo Fisher Scientific) electron microscope operated at 300 kV. The data acquisition was performed at a nominal magnification of 75,000× with a Falcon 4i direct electron detector (Thermo Fisher Scientific). All datasets were recorded with an accumulated total dose of 50 $e^-/Å^2$ and the exposures were fractionated into 50 frames. The targeted defocus values ranged from -0.25 to -2.5 mm. For the BAF-$OS^{-6.0}$ complex, 20,104 EER movies were recorded. For the BAF-$OS^{+6.0}$ complex, 39,572 EER movies were

recorded. A subset of 16,394 movies were recorded with the stage tilted to 30 degrees. For the BAF-OS$^{+6.0\ ADP}$ complex two sessions with a total of 18,456 EER movies were recorded. For all datasets, the raw EER movies were grouped into 50 frames and converted to 4k LZW-TIFF using *relion_convert_to_tiff*.

Cryo-EM data processing

Real-time evaluation along with acquisition with EPU (Thermo Fisher Scientific) was performed with CryoFLARE.[76] Within CryoFLARE, drift correction was performed with the *Relion motioncor implementation*,[97] where a motion corrected sum of all frames was generated with and without applying a dose weighting scheme. CTF was fitted using GCTF[98] on the non-dose-weighted sums. After CTF estimation, only the data that showed a CTF fit better than 5 Å was exported from CryoFLARE and used for further processing with Warp[77], Relion[78] and cryoSPARC.[79]

For the BAF-OS$^{-6.0}$ complex, the raw movies were imported into Warp and subjected to patch motion correction, ctf fitting and particle picking. Two rounds of 2D classification were used to remove bad particles from the datasets. *Ab-initio* reconstruction (four classes) followed by heterogeneous refinement were performed to obtain an initial three-dimensional model at 4.1 Å (147,556 particles). This reconstruction was used as a seed model (six times) for one round of heterogeneous refinement using all the particles initially picked in Warp (1,744,128 particles). In the attempt to improve the local EM densities for OCT4-SOX2 and the BASE module, the data processing followed two distinct paths. First, the largest class with 371,823 particles showed unambiguous density for OCT4-SOX2 and was used to obtain a consensus map at 3.2 Å resolution. 3D focus classification (eight classes) followed by particle subtraction and local refinement around the nucleosome-OCT4-SOX2 part of the complex led to a structure at 3.2 Å resolution (46,160 particles), where the TFs bind in a similar fashion as the same assembly in isolation (i.e., without the BAF remodeler, PDB: 6t90). Second, the best two classes (670,056 particles) showing defined density for the BASE module were selected and further homogeneous refinement led to a consensus map at 4.1 Å resolution. To improve the BASE part of the complex, 3D focus classification (four classes) followed by non-uniform refinement from the 670,056-particle subset led to a consensus structure at 3.5 Å resolution (179,373 particles). Further BASE EM density improvement was obtained with local refinement, leading to a BASE structure at 3.1 Å resolution. Likewise, further density improvement on the nucleosome via local refinement led to a nucleosome-focused map at 2.9 Å resolution. To improve the ARP part of the complex, a mask including ARP and the ATPase was used in 3D focus classification (ten classes) were the best two classes (129,082 particles) showing clear EM density for ARP were selected for further processing using homogeneous refinement, leading to a consensus structure at 5.6 Å resolution. Particle subtraction, re-window particles to a smaller box size (from 480 pixels to 360 pixels) and local refinement around the ARP part of the complex led to a structure at 3.7 Å resolution.

For the BAF-OS$^{+6.0\ AMP\text{-}PNP}$ complex, the drift corrected averages were imported into Warp and subjected to patch ctf fitting and particle picking. The data from the tilted and untilted stage were initially processed with two independent Warp sessions. After importing the corresponding particles into cryoSPARC, four rounds of 2D classification were used to remove bad particles. To improve the homogeneity of the dataset, *ab-initio* reconstruction (four classes) followed by heterogeneous refinement were performed on 442,529 and 311,094 particles for the zero- and 30-degree tilt subsets respectively. Both subsets revealed the presence of two complex conformations, labeled as class 1 and class 2 (Figures S5 and S7). All class 1 particles were merged, and homogeneous refinement gave rise to a consensus map with an overall resolution of 3.1 Å. 3D classification into 10 classes improved the EM density around the OCT4-SOX2 region. Particles included in the best class were imported into Relion for one round of 3D focused classification using a soft mask around the nucleosome-OCT4-SOX2 region. The particles included in the most populated class (84%) were finally re-imported into cryoSPARC to perform 3D flexible refinement,[67] which confirmed the high degree of flexibility present in this protein assembly. All class 2 particles were merged and subjected to heterogeneous refinement leading to a consensus map at 4.2 Å resolution (30,808 particles). Local refinement was used to improve the EM densities for the ARP-BASE and the nucleosome-OCT4/SOX2-ATPase modules separately.

For the BAF-OS$^{+6.0\ ADP}$ complex, the drift corrected averages were imported into Warp and subjected to patch ctf fitting and particle picking. After importing the corresponding particles into cryoSPARC, three rounds of 2D classification were done and particles from unambiguously distinguishable 2D classes were assigned either as class 1 and 2 type particles or as class 3 type particles. *Ab-initio* was used to separately reconstruct the conformational classes, and several 3D classes of each conformation were considered for further processing. Noise traps (K=12 classes) were generated from particles unaligned in 2D classification and used together with the eight reconstructions representative of all BAF classes as inputs for further refinement and class separation. The volumes (BAF classes and noise traps) were used as input in heterogeneous refinement using all the particles (2,420,264) initially picked in Warp. Particles clustering with either class 1 and 2 or class 3 type BAF conformations were merged with previously assigned particles of the same type and analyzed by 2D classification (2 rounds). Particles that changed class type were re-analyzed by 2D classification (2 rounds) separately and re-assigned accordingly. *Ab-initio* reconstitutions of each type 1,2 or 3 final particle stacks (after 2D classification) were performed separately for each class type including generation of noise traps representative of the particle clustered in each BAF class type. Another heterogenous refinement was performed within each BAF class type 1 and 2 or 3 separately, together with their respective noise traps and particles clustering with BAF classes were re-analyzed by 2D classification (1 round) and selected distinguishable BAF classes were merged with the final particle stack. Additionally, particles that did not align in 2D classification but had a 3D-class probability of a given BAF 3D class higher than 99.9% were also merged to the final particle stack of the respective BAF class type resulting in 145,519 (37.1%) BAF class 3 and 246,791 (62.9%) BAF class 1 and 2 particles. *Ab-initio* (K=5) of the final class 3 type particle stack resulted in three full reconstructions that were subjected to distinct processing paths to improve

the EM densities for either the OCT4/SOX2 TFs, the ATPase or the BASE module respectively based on initial EM densities for each respective parts in *ab-initio*. 3D-classification, focused on the OCT4/SOX2 TFs revealed classes (Figure S9E) where OCT4/SOX2 density is clearly resolved. Non-Uniform and local refinement, focused on the NCP-ATPase was used to improve the final EM maps, giving reconstructions at 3.95 Å and 4.05 Å respectively (Figure S9F). Non-Uniform and local refinement, focused on the BASE module was used to improve the final EM maps, giving reconstructions at 5.93 and 6.49 Å respectively (Figure S9H) with the latter shown in two different orientations. Maps stemming from the focus-refined maps of the NCP-ATPase (4.05 Å) and BASE module (6.49 Å) respectively were merged to a composite map.

Structural model building and structural analysis

Model coordinates for BAF were extracted from PDB ID 6ltj and fitted together with OCT4/SOX2-bound nucleosome (PDB: 6t90) into the cryo-EM map using ChimeraX fit-in-map.[80] The structure of pBAF (PDB: 7vdt) including parts of the BRG1 SnAC domain was aligned using the nucleosome as reference and the SnAC domain was copied into the BAF-OS$^{-6.0}$ model. The SMARCD1 YEATS-like domain was derived from a predicted model (AlphaFold database, AF-Q96GM5-F1) and rigid-body fitted into the cryo-EM map as above. Chains were trimmed or extended based on available density using COOT[81] and corresponding predictions from the AlphaFold database. The models were combined and subjected to MDFF (Molecular Dynamics Flexible Fitting) in ISOLDE.[82] Throughout MDFF self-restraints were employed. Finally, PHENIX real-space refinement was used to minimize the model coordinates (in the presence of coordinate constraints).[84] Model B-factors were refined with Rosetta (BfactorFitting Mover[85]). Molprobity was used for validation.[86]

To obtain a model for BAF-OS$^{+6.0}$ (class 2), the previous BAF-OS$^{-6.0}$ model was used as template and the nucleosome coordinates were replaced by SHL+6-OCT4/SOX2-bound nucleosome (PDB: 6yov). Due to low local resolution, the BRG1 C-terminal lobe was omitted from the model. Further refinement and validation of the model was as described above. In case of BAF-OS$^{+6.0}$ (class 1), BAF-OS$^{+6.0}$ (class 2) was used as template and BAF was re-fitted in ChimeraX. Refinement was again as described before. Map and model representations in the figures were prepared using UCSF ChimeraX.

In case of BAF-OS$^{+6.0\ ADP}$ (class 3), the ATPase lobes of BRG1 were extracted from pBAF (PDB: 7vdt) and for the remaining model, BAF-OS$^{+6.0}$ (class 1) was used as template. Subunits were rigid body-fitted followed by refinement and validation as described above. The structures were analyzed using UCSF Chimera,[87] UCSF ChimeraX,[80] and Pymol.

QUANTIFICATION AND STATISTICAL ANALYSIS

Statistical analysis of restriction enzyme-based remodeling assays

Gel images were analyzed using ImageJ[88] by measuring the intensities of uncut DNA bands. For each condition, values were normalized to the uncut band in the absence of remodeler or transcription factor, which served as the 100% reference, allowing calculation of the relative change in cutting rate. Statistical comparisons between conditions were performed using an unpaired two-tailed Student's *t*-test, based on three technical replicates per measurement (n=3). *P*-values are indicated as $p < 0.05$ (*) and $p < 0.01$ (**). All bar graphs display mean values ± standard deviation (SD).

Statistical analysis of ensemble FRET-based remodeling experiments

For ensemble FRET experiments, fluorescence signals were recorded continuously during the reaction. Baseline FRET efficiencies were determined as the mean value over a 1-minute period preceding reaction initiation by addition of BAF. FRET efficiencies following nucleosome remodeling were determined as the mean value over a 1-minute window at 20 minutes after reaction start. For each condition, mean FRET efficiencies were calculated from three independent replicates (n=3). Data are presented as mean ± standard deviation (SD). Statistical significance between conditions was assessed using an unpaired two-tailed Student's *t*-test. A p-value < 0.05 was considered statistically significant.